High Temperature magnetic properties of transition metal oxides with perovskite structure

Dinesh Baskar

A dissertation submitted in partial fulfillment of
the requirements for the degree of

Doctor of Philosophy

University of Washington

2008

Program Authorized to Offer Degree:
Department of Chemical Engineering

ProQuest LLC
789 E. Eisenhower Parkway
PO Box 1346
Ann Arbor, MI 48106-1346

University of Washington

Graduate School

This is to certify that I have examined this copy of a doctoral dissertation by

Dinesh Baskar

and have found that it is complete and satisfactory in all respects,
and that any and all revisions required by the final
examining committee have been made.

Chair of the Supervisory Committee:

Stuart B.Adler

Reading Committee:

Stuart B.Adler

Daniel T.Schwartz

Guozhong Cao

Date: 6/12/08

Signature____________________

Date 6/18/08

University of Washington

Abstract

High Temperature magnetic properties of transition metal oxides with perovskite structure

Dinesh Baskar

Chair of the Supervisory Committee:
Professor Stuart B.Adler
Department of Chemical Engineering

In recent years, transition metal oxides with perovskite structure have drawn considerable interest as mixed ionic electronic conductors (MIECs) that can conduct electrons and ions at high temperatures. Many phenomena of interest in perovskites occur at high temperature including electronic and ionic transport, catalysis and chemical expansion. Electronic structure controls host of critical properties that are of technological importance including oxygen nonstoichiometry, electronic and ionic conductivity.

In this work, we have designed an experimental method to measure magnetization of transition metal oxide perovskites at high temperatures (600^0C - 1000^0C) as a function of oxygen partial pressure. High temperature magnetic measurements were used to study electronic structure in two promising transition metal oxide perovskites for intermediate temperature solid oxide fuel cells: $La_{1-x}Sr_xCoO_{3-\delta}$(LSC) and $La_{1-x}Sr_xFeO_{3-\delta}$(LSF). LSF has semiconducting behavior and many of its properties have been attributed to change in oxidation state of iron with changes in temperature and oxygen partial pressure. LSC, on the other hand, has many properties that point towards metallic behavior at high temperatures.

temperature and oxygen partial pressure. LSC, on the other hand, has many properties that point towards metallic behavior at high temperatures.

We find that at high temperatures, the oxygen nonstoichiometry and temperature dependence of magnetic susceptibility could be explained within the framework of localized electronic defects for LSF. In Contrast, the magnetic property of LSC at high temperatures suggest co-existence of localized and delocalized electronic states. We discuss this behavior in the context of existing electronic structure models, as well as transport properties.

TABLE OF CONTENTS

Page

List of Figures iii

List of Tables vi

Chapter 1. Introduction 1

1.1 Motivation 1
1.2 $La_{1-x}Sr_xCoO_{3-\delta}$ (LSC): Literature Review 6
1.3 $La_{1-x}Sr_xFeO_{3-\delta}$ (LSF): Literature review 8
1.4 Present Work 10

Chapter 2. Electronic structure and magnetic properties 12

2.1 Introduction 12
2.2 Paramagnetic materials 17
  2.2.1 Localized electrons 17
  2.2.2 Delocalized (band)electrons 19
2.3 Magnetization measurement methods 22
  2.3.1 Induction method 22
  2.3.2 Force methods: 23
2.4 Summary 24

Chapter 3. High temperature Faraday Magnetometer 26

3.1 Introduction 26
3.2 Instrument Design 27
  3.2.1 Tilt correction for stray gradient field 32
3.3 Instrument Performance 36
3.4 Summary 44

Chapter 4. Oxygen nonstoichiometry: Thermodynamic models 45

4.1 Introduction 45
4.2 Thermodynamic properties of LSF 46
4.3 Thermodynamic properties of LSC 50
4.4 Summary 58

Chapter 5. High temperature magnetic property of LSF 60

5.1 Introduction 60

5.2 Experimental details 62
5.3 Results and discussion 62
5.4 Summary 69

Chapter 6. High temperature magnetic properties of LSC 70

6.1 Introduction 70
6.2 Experimental details 70
6.2.1 Sample preparation and characterization 70
6.3 Results and Discussion 74
6.3.1 Low temperature magnetization 74
6.3.2 High temperature magnetization 76
6.4 Summary 89

Chapter 7. Modification of rigid electron band model to predict oxygen vacancies in LSC 91

7.1 Introduction 91
7.2 Rigid band model: Review 92
7.3 Modifications to rigid band model 97
7.4 Summary 106

Chapter 8. Conclusions and Future directions 107

References 114

LIST OF FIGURES

Figure Number Page

1-1. Ideal cubic perovskite lattice with oxygen vacancies 2

2-1: types of ordered magnetic materials 15

2-2: Behavior of localized electrons. 18

2-3: Behavior of delocalized electrons 21

3-1: Cross-sectional schematic of the instrument assembly 30

3-2: Cross section of the furnace–cooling jacket assembly 31

3-3: (a) Components of the Cahn microbalance. (b) Force diagram for the balance beam inclined at an angle α .(c) Schematic of stray field component reduction by the introduction of angle α. 35

3-4: (a) Force signal due to stray magnetic field, ΔS for different sample mass (m_s) and tare mass (m_t) combinations (b) ΔS for different values of torque at an angle of 7.6 degrees. 37

3-5: Magnetic force signal measured at different temperatures for (a) Alumina (b) LSC 3710 41

3-6: Magnetic force signal for LSC 6410 42

3-7: Magnetic susceptibility of LSC 6410 43

4-1: Oxygen nonstoichiometry of LSF (x =0.1) from literature[61] 47

4-2: Hopping mechanism for conductivity in LSF 47

4-3: Nonstoichiometry behavior of LSF 48

4-4: Oxygen nonstoichiometry behavior of LSC -73 from literature[47]. 51

4-5: Rigid electron band model 53

4-6: Oxygen nonstoichiometry values for LSC (x=0.2) 55

4-7: Oxygen nonstoichiometry values for LSC (x=0.4) 56

4-8: Oxygen nonstoichiometry values for LSC (x=0.7) 57

5-1: Magnetic susceptibility of LSF 8210 66

5-2: Magnetic susceptibility of LSF 6410 67

5-3: (a) Magnetic interaction parameter, λ for LSF at different temperatures as a function of oxygen non-stoichiometry. (b) Ordering temperature, θ corresponding to lambda values as a function of nonstoichiometry. 67

5-4: Magnetic interaction parameter, λ for LSF-64 at different temperatures as a function of oxygen nonstoichiometry. 68

5-5: Parameter, λ, as a function of (a) oxygen nonstoichiometry and (b) electron occupancy. 68

6-1: XRD pattern of as-sintered LSC 6410 72

6-2: XRD pattern of LSC 6410 quenched at 900 °C and 100 ppm ($\delta = 0.27$) 72

6-3: Low temperature magnetization (FC and ZFC) for LSC-64 75

6-4: Plot of ordering temperature as a function of oxygen vacancy concentration 75

6-5: High temperature magnetic susceptibility of LSC 77

6-6: Electrical resistivity of LSC 78

6-7: Schematic of the electronic structure of LSC 82

6-8: Activation energy plot for conductivity 83

6-9: Contribution of defect scattering to electrical resistivity 85

6-10: Estimated number of Bohr magnetons for LSC 87

6-11: Magnetic susceptibility of LSC-37 at intermediate temperatures 89

7-1: Enthalpy of oxidation as a function of oxygen nonstoichiometry 96

LIST OF TABLES

Table Number Page

2-1 Magnetic behavior versus values of magnetic susceptibility 16

2-2 Curie and Néel temperatures of some Lanthanides 16

4-1 Fitting parameters used for experimental data 58

7-1 Thermodynamic data for $La_{0.6}Sr_{0.4}CoO_{3-\delta}$ 95

7-2 Parameters from data fitting using modified rigid band model 103

ACKNOWLEDGEMENTS

I am very grateful to many people who have contributed greatly to my graduate school experience. I offer my sincere thanks to my advisor Professor Stuart B.Adler, under whose direction I had the great learning experience and appreciation for fine details in research. I also express my gratitude to my committee members Dr. Daniel T.Schwartz and Guozhong Cao, for their feedback and support. I also express my thanks to the members, past and present of the Adler group.

I am grateful for my friends and family, who have been a continual source of encouragement and inspiration. I also acknowledge the support of Dave Gery, Arnie Biermans, Valentine Medvedev and David Englert for their assistance with various aspects of the instrument design, which is a central part of this work. Finally, I would like to thank National Science Foundation (NSF) for providing funding for my research.

DEDICATION

To my Family

Chapter 1. Introduction

1.1 Motivation

Transition metal oxides with perovskite structure ($ABO_{3-\delta}$, B-transition metal, A-rare earth metal, δ – oxygen vacancy) encompass a variety of present technologies including spin-tronics, high-T_C superconductors, gas sensors and separation membranes, and solid oxide fuel cell (SOFC) electrodes[1-6]. In recent years, perovskite oxides have drawn considerable interest as mixed ionic electronic conductors (MIECs) that can conduct electrons and ions at high temperatures. MIECs show substantial improvement in electrode performance compared to pure electronic conductors[5, 7]. Initial studies of perovskite MIEC electrodes showed better kinetic properties than Pt in the temperature range 1000 – 1100^{0}C. Higher electronic conduction is often correlated with faster oxygen exchange in MIECs; high concentrations of mobile electronic carriers display better surface catalytic properties than ionically conductive materials.[8, 9]

Perovskites display a wide array of properties depending upon the constituent ions in the structure. For example, $BaTiO_3$ is ferroelectric and an insulator, $BaBiO_3$ is an insulator, and $LaTiO_3$ and $LaNiO_3$ are metallic. Many of these observed properties could be altered by either doping A-site and/or B-site cations, e.g: introduction of Pb for Bi leads to high Tc superconductor behavior[10, 11] in $BaBiO_3$. An ideal cubic perovskite structure is shown in Figure 1.1. A-site cations occupy the corners of the unit cell, while smaller B-site cation occupies the body center of the cubic lattice. Oxygen anions are in the face centered sites of the cubic lattice; each unit cell consists of 1 A-site cation, 1 B-site cation and 3 oxygen anions. The valence states of the A-site and B-site cations are particular to the perovskite material. For example, in barium titanate, BaTiO$_3$, the A-site barium has +2 valance and B-site titanium cation has a +4 valance compared to LaCoO$_3$ where both lanthanum and cobalt have +3 valance state.

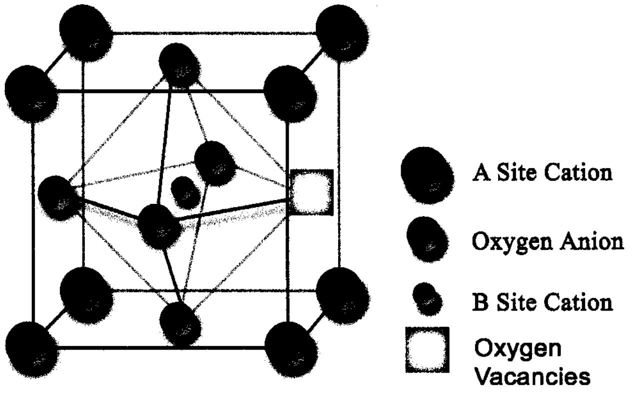

Figure 1-1. Ideal cubic perovskite lattice with oxygen vacancies

The unique properties of perovskite oxides are closely related to the defect chemistry involved. It is common to have more than one type of cation in A-site and B-site lattice, to enhance the defect concentration. Most commonly used perovskite oxides in the above stated applications are of the type La$_{1-x}$Sr$_x$MO$_{3-\delta}$, where M is a transition metal cation such as Cr, Co, Fe and/or Mn. [1, 6, 11-13] In this type, La^{+3} is doped with Sr^{+2} ions and occupy A-site, and M (=Co, Cr, Fe, or Mn) ions occupy the B-site. Upon the substitution of strontium for lanthanum, the difference in ionic charge between Sr^{2+} and La^{3+} must be compensated. Oxidation of other species in the structure, such as Co^{3+} to Co^{4+}, or a creation of oxygen vacancy ($\delta > 0$) can balance the charge. Changes in oxidation state of ions can aid in hopping type conduction where electrons/holes can be transported from one site to the other. Oxygen vacancies provide pathway for oxygen ionic transport and also aid in adsorption of oxygen gas onto the surface of perovskite oxide[14-17].

Perovskite oxides of type $La_{1-x}Sr_xMO_{3-\delta}$ is of particular interest due to its ability to support high defect concentrations at reduced temperatures (less than 800°C).[8] One of the active areas of interest is to develop materials that retain the useful properties, yet operate at temperatures less than 600°C [18-20]. However, many properties of these materials including electrical conductivity, oxygen nonstoichiometry, and Seebeck coefficient are strongly a function of temperature, oxygen partial pressure and dopant concentration[12, 21-25]. For example, $La_{1-x}Sr_xCoO_{3-\delta}$ is metallic and supports large concentrations of vacancies at temperatures above 700°C while it is an insulator at low temperatures[23]. One of the primary issues in intermediate temperature solid oxide fuel cells is that cathode performance decreases with lower operating temperature[26]. Even in the widely used electrode material $La_{1-x}Sr_xMnO_3$, the performance is lowered significantly by reducing the operating temperature[27]. Some oxides with perovskite undergo transition from insulator at room temperature to metallic conductor at high temperatures. Although the range of conditions over which this transition occurs has been identified, the mechanism through which this transition takes place is still an open question in the literature[21, 28-32].

In order to understand these transitions in observed property, we have to address the issue of electronic structure in these materials. Electronic structure is closely related to a host of critical material properties including electron and ionic transport, catalytic activity, thermodynamic and kinetic stability, chemical expansion and stress. Electronic structure is usually understood from two fundamentally different approaches[10, 29, 33]. In one approach that includes ionic models and crystal field theory, electrons are considered as localized charges or point defects associated with particular atoms or group of atoms. This viewpoint of electronic structure works well for explaining hopping type conductivity and point defect chemistry. In the second approach, which includes band theory, electrons are considered to be wave functions that occupy electron energy bands associated with a periodic lattice. This approach helps in explaining magnetic ordering behavior, Peirls instability and other co-operative phenomena[10, 29, 33].

However, most properties of interest in mixed conducting perovskites cannot be explained using one particular approach due to complex atomic and electronic ordering of intermediate length scales. Most perovskite oxides are found to be spatially inhomogeneous on an intermediate length scale using neutron diffraction studies, even though XRD studies showed long range cubic symmetry[28, 34-36]. Electronic structure inhomogeniety has been observed from spectroscopic measurements, suggesting the presence of ferromagnetic and paramagnetic phases at low temperatures[37-40]. Little information is known about the effect of these inhomogeneities on the observed properties of perovskites. High temperature nuclear magnetic resonance (NMR) suggests coexistence of delocalized magnetic bands with localized unpaired spins[28]. Evidence for local magnetic domains persisting at high temperature has been observed using ^{La}NMR (nuclear magnetic resonance) measurements[41].

While the existing models of electronic structure provide useful directions, we must invoke a mixture of localized and cooperative arguments to explain the observed properties in perovskites. Methods commonly used to understand electronic structure include electrical conductivity and Seebeck coefficient measurement, spectroscopic techniques (XPS, XAFS, Mossbauer) and ^{17}O nuclear magnetic resonance (NMR) method[28, 42-44]. This work focuses on introducing a method to probe the electronic structure using magnetic property measurement at high temperatures (> 700^{0}C). This is done in conjunction with electrical conductivity measurement and low temperature magnetic property studies. We are interested in the electronic and transport properties of highly defective perovskite oxides such as $La_{1-x}Sr_xMO_{3-\delta}$ (M = Co, Fe).

$La_{1-x}Sr_xCoO_{3-\delta}$ (LSC) and $La_{1-x}Sr_xFeO_{3-\delta}$(LSF) are two materials of interest for intermediate temperature solid oxide fuel cell[6, 9, 20]. $La_{1-x}Sr_xMnO_{3-\delta}$ (LSM) is the cathode material of choice for commercial use due to its compatibility with yttria doped ceria (YSZ), a widely used electrolyte material. However, LSM is a poor ionic conductor at reduced temperatures which restricts the application to high temperatures. Preliminary measurements of cell performance using LSC and LSF as cathode materials with YSZ or gadolinia doped ceria (GDC) electrolyte shows promising results at intermediate temperatures. Section 1.3 and Section 1.4 provide a brief introduction to high temperature properties of $La_{1-x}Sr_xCoO_{3-\delta}$ and $La_{1-x}Sr_xFeO_{3-\delta}$, respectively. Section 1.5 summarizes the organization of the present work.

1.2 $La_{1-x}Sr_xCoO_{3-\delta}$ (LSC): Literature Review

$La_{1-x}Sr_xCoO_{3-\delta}$ (LSC) has enjoyed particular attention because of its ability to become reduced at moderate P_{O2}, producing high concentrations of oxygen ion vacancies in air [1, 45-48]. The high-temperature thermodynamic, transport, and catalytic properties of LSC have often been attributed to its high oxygen vacancy concentration, as well as metallic band structure, which appears to prevail at high temperature[49]. Previous electronic conductivity and Seebeck measurements of LSC suggest that it undergoes a broad semiconductor-to-metal transition as a function of temperature, with the transition temperature being strongly dependent on Sr doping (x)[23, 32, 50]. The parent oxide, $LaCoO_3$, is a semiconductor with rhombohedral structure at room temperature. The substitution of La^{3+} with Sr^{2+} reduces the rhombohedral distortion by Co-O octahedral tilting and it reaches cubic structure for $x > 0.5$[35, 36]. Introduction of effective negative charges, due to difference in valance between La and Sr, leads to increased electronic charge carriers. Its has been shown that the cubic phase of LSC shows metallic conductivity, while the rhombohedral phase shows semiconducting behavior[23, 38].

The electrical conductivity at room temperature generally increases with increase in Sr content with maximum at $x = 0.5$, and decreases thereafter. This change in electrical conductivity variation with Sr content, referred to as the metal-insulator transition (MIT), is extensively studied using crystallographic methods [22, 32, 36, 44, 51]. It was observed that a contraction of the Co-O distance and an expansion of Co-O-Co angle happen at $x \cong 0.25$ in LSC, at which the conduction state changes from insulating (semiconducting) to metallic. However, the transition temperature predicted by cystrallographic studies is much higher than actual observed transition temperature based on conductivity measurements.

Another explanation for the metal-insulator transition in LSC, is based on spin configuration of cobalt and its changes with temperature. MIT is often times correlated with changes in spin state of Cobalt with temperature and oxidation state, based on ab-initio calculations and/or by measurement of lattice volume changes. Liu and coworkers[52] claimed that at $x > 0.125$, the LSC system becomes ferromagnetic due to the Co^{4+}-O-Co^{3+} exchange interaction. This ferromagnetic interaction, prevailing at low temperature, is compensated by temperature increase due to oxygen content changes resulting in individual spin alignment. [52] Theotretical models, predict that Co transitions from LS to IS to HS as a function of temperature and oxidation state. Even in the low temperature regime (<500^0C), the spin state of Cobalt ions is still a matter of debate[38, 53-57]. The cobalt spin state has never been measured at high temperature, particularly as a function of Co oxidation state.

1.3 $La_{1-x}Sr_xFeO_{3-\delta}$ (LSF): Literature review

$La_{1-x}Sr_xFeO_{3-\delta}$ (LSF) has been studied for the past few decades as a leading candidate for solid oxide fuel cell cathode material. LSF shows better thermal expansion coefficient match with electrolytes while maintaining high mixed conductivity and good catalytic activity for oxygen reduction[5]. In addition, LSF tends to react more slowly with the yttria stabilized zirconia (YSZ) electrolyte than LSM and LSC at the operating conditions of solid oxide fuel cells. The unique electrical properties associated with LSF are closely coupled with the defect chemistry[58-61].

The electrical conductivity and Seebeck coefficients of LSF were measured as a function of oxygen partial at different temperature by Mizusaki [59]and Yoo [62]. The electrical conduction was p-type in the higher P_{O2} range, and n-type in the lower P_{O2} range. The Seebeck coefficient indicated that the conduction was due to electron hopping between Fe^{3+} and Fe^{4+} at higher P_{O2} and electron hopping between Fe^{2+} and Fe^{3+} in the lower P_{O2} range. Hence, LSF undergoes a transition from n-type to p-type with increase in oxygen partial pressure at high temperatures. Based on this observation, Mizusaki proposed a thermodynamic model using mass action equilibria for oxygen vacancies, oxidation states of iron and strontium composition. This model [61]correctly predicts n-type and p-type regimes at high and low P_{O2}, respectively, with a power law dependence of oxygen vacancy concentration on P_{O2}

Previous studies of electrical and magnetic properties of $La_{1-x}Sr_xFeO_3$ suggest strong correlation between Sr-doping levels and observed properties. The oxygen nonstoichiometry in $La_{1-x}Sr_xFeO_{3-\delta}$ was found to play an important role in the magnetic structure of samples quenched from various gas atmospheres. Magnetic property of LSF is closely related to the oxygen vacancy concentration and oxidation state of iron. An early Mossbauer spectroscopic studies in LSF at room temperature identified different characteristics for Fe^{4+} and Fe^{3+} at large values of *x*[63]. Interest in coupling between transport and magnetic properties of LSF has been simulated by a variety of applications such as colossal magnetoresistance (CMR) and spintronic applications. The magnetic ordering is thought to arise from a superexchange interaction between the 3d orbital of transition metal ions and the 2p orbital of oxygen ions[39, 64, 65]. Therefore, the magnetic property (or magnetic moments) will mainly be determined by the number of unpaired 3d electrons on transition metal cations.

At high temperatures, the concentration of oxygen vacancy in the system increases leading to change in the magnetic interaction. However, most of the current measurements of magnetic property were done at temperatures less than 500^0C[39, 64, 65]. In some cases, the neutron scattering measurements were done on quenched samples to identify the effect of oxygen vacancies on the nature of magnetic interaction. High temperature magnetic property studies, in-situ, can provide information about the behavior of localized electrons. These measurements can offer insight regarding the nature of magnetic interaction as a function of oxygen vacancy concentration.

1.4 Present Work

One of the major focuses of this work is to develop a measurement technique that aids in quantifying the localized electrons and delocalized electronic states in electrochemical oxides. This thesis presents a working design of the high temperature Faraday balance capable of measuring magnetic susceptibility of a sample as a function of temperature and oxygen vacancy concentration. In order to address electronic structure issues, we have measured magnetic susceptibility as a function of T and P_{O2} which allows us to control oxidation state of transition metal cations *via* equilibrium with the gas.

By quantifying changes in magnetic susceptibility with temperature and oxidation state independently, this technique gives insight into whether electron states (filled or depleted) at the Fermi level are localized or delocalized, as well as whether localized unpaired spin states remain within the metallic state at high temperatures. We have studied two of the most promising mixed ionic electronic conducting oxides: LSC and LSF using this method. We have also extended previous measurements of electronic conductivity as a function of P_{O2} and T *in* order to delineate changes in electronic structure from changes in carrier concentration.

Chapter 2 presents a brief introduction to various magnetic materials and the commonly used magnetization measurement principles. Chapter 2 also highlights the theoretical background to explain the difference in magnetic susceptibility of localized and delocalized electrons. Chapter 3 discusses the working design of a high temperature Faraday magnetometer along with preliminary measurements, which show the effectiveness of the Magnetometer to measure magnetic susceptibility as a function of temperature and defect concentration in the samples. In chapter 4, we present the commonly used thermodynamic models to calculate the oxygen defect concentrations in LSF and LSC from literature. These models can be helpful in predicting oxygen defect concentration in the samples at the temperature and oxygen partial pressure of interest, based on fitting parameters.

Chapters 5 and 6 present the high temperature magnetic susceptibility results for LSF and LSC respectively. We discuss the magnetic behavior in comparison with measured electrical conductivity and existing models of electronic structure. In Chapter 7, we present a thermodynamic model for LSC based on our understanding of electronic structure from magnetic measurements. Lastly, Chapter 8 presents the conclusions and future directions of this work.

Chapter 2. Electronic structure and magnetic properties

2.1 Introduction

When a material is placed within a magnetic field, the magnetic forces of the material's electrons will be affected. However, materials can react quite differently to the presence of an external magnetic field. This reaction is dependent on a number of factors, such as the atomic and molecular structure of the material, and the net magnetic field associated with the atoms[66, 67]. The magnetic moments associated with atoms have three origins: 1) electron orbital motion 2) the change in orbital motion caused by an external magnetic field, and 3) spin of the electrons. In most atoms, electrons occur in pairs and their opposite spins cause their magnetic fields to cancel each other. Therefore, no net magnetic field exists. Alternately, materials with some unpaired electrons will have a net magnetic field and will react more to an external field.

The magnetic behavior of materials can be classified into five major groups: 1) Diamagnetism 2) Paramagnetism 3) Ferromagnetism 4) Antiferromagnetism, and 5) Ferrimagnetism. Materials in the first two groups are those that exhibit no collective magnetic interaction of atomic magnetic moments and are not magnetically ordered. Materials in the last three groups exhibit long-range magnetic order between atomic moments below a certain critical temperature.

Diamagnetic metals have a very weak and negative susceptibility to magnetic fields. Diamagnetic materials are repelled by a magnetic field and the material does not retain the magnetic properties when the external field is removed. Diamagnetic materials are solids with all paired electrons resulting in no permanent net magnetic moment per atom. Diamagnetic properties arise from the realignment of the electron orbits under the influence of an external magnetic field. Most elements in the periodic table (ex: copper, silver, and aluminium), are diamagnetic. Magnetic properties other than diamagnetism, which is present in all substances, arise from the interactions of unpaired electrons. These properties are traditionally found in transition metals, lanthanides, and their compounds due to the unpaired d-oribital and f-orbital electrons on the metal.

Ferromagnetic materials become magnetized when the magnetic domains within the material are aligned. This can be done by placing the material in a strong external magnetic field or by passing electrical current through the material. Some or all of the domains can become aligned. The more domains that are aligned, the stronger the magnetic field in the material. When all of the domains are aligned, the material is said to be magnetically saturated, as shown in Fig 2.1a. When a material is magnetically saturated, no additional amount of external magnetization force will cause an increase in its internal level of magnetization. In ionic compounds, such as oxides, more complex forms of magnetic ordering can occur as a result of the crystal structure. One type of magnetic ordering is called **ferrimagnetism**, a simple representation of magnetic spins in ferromagnetic oxide is shown in Fig 2.1b. The magnetic structure is composed of two magnetic sublattices (called A and B) separated by oxygens. The exchange interactions are mediated by the oxygen anions. When this happens, the interactions are called indirect or superexchange interactions. The strongest superexchange interactions result in an antiparallel alignment of spins between the A and B sublattice. In ferrimagnets, the magnetic moments of the A and B sublattices are not equal and result in a net magnetic moment. If the A and B sublattice moments are exactly equal but opposite (as shown in Fig 2.1c), the net moment is zero. This type of magnetic ordering is called antiferromagnetism. Magnetic character of materials is typically analyzed relative to its magnetic susceptibility (χ). Magnetic susceptibility is the ratio of magnetization, M (defined as the magnetic moment per unit volume) to magnetic field (B).

Paramagnetic materials have a net magnetic moment due to unpaired electrons in partially filled orbitals. However, the individual magnetic moments do not interact magnetically, and like diamagnetism, the magnetization is zero when the field is removed. In the presence of a field, there is a partial alignment of the atomic magnetic moments in the direction of the field, resulting in a net positive magnetization. The typical values of χ for these classes of magnetic materials are shown in Table 2-1. Ferromagnetic and antiferromagnetic materials will lose magnetic character and become paramagnetic if sufficiently heated. The temperature at which this occurs is defined as the Curie temperature (T_c) for ferromagnetic compounds and the Néel temperature (T_N)

for antiferromagnetic compounds. Some substances, particularly the later lanthanides, will go from paramagnetic to antiferromagnetic to ferromagnetic as temperature decreases. Curie temperature and Néel temperature for some of the lanthanide series elements from literature [68] are shown in Table 2-2.

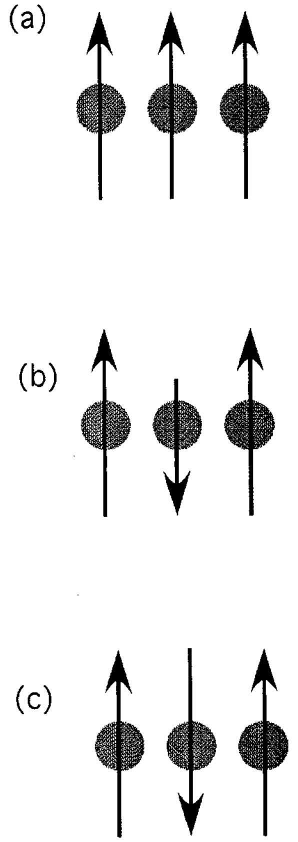

Figure 2-1: Types of ordered magnetic materials (a) Ferromagnetism (b) Ferrimagnetism and (c) Antiferromagnetism

Table 2-1: Magnetic behavior versus values of magnetic susceptibility

Magnetic behavior	**Value of χ**
Diamagnetic	Small and negative
Paramagnetic	Small and positive
Ferromagnetic	Large and positive
Antiferromagnetic	Small and positive

Table 2-2: Curie and Néel temperatures of some Lanthanides[68].

Metal	**Curie Temperature, T_C (°C)**	**Néel Temperature, T_N (°C)**
Cerium (Ce)	-	-260.65
Samarium (Sm)	-	-258.35
Gadolinium (Gd)	20	-
Hofnium (Ho)	-253	-142

2.2 *Paramagnetic materials*

At high temperatures, most magnetically ordered materials are paramagnetic. However, the temperature dependence of paramagnetic materials depends on the nature of electrons: metallic or localized[66, 67].

2.2.1 Localized electrons

An atom with angular momentum quantum number j has the degeneracy of 2j+1 and when a magnetic field is applied the degeneracy is removed resulting in equally spaced levels of energy $gJ\mu_B$. For the simplest case, j = 1/2, this phenomenon is illustrated in Fig 2.2. This split in energy levels is of the order of kT, hence temperature changes can cause fluctuations in population of electrons in these energy states. The net magnetization will be determined by the difference in population of electrons in these two levels. The net magnetization is given by:

$$M = NgJ\mu_B B_J(x)\text{, where } x = \frac{gJ\mu_B B}{kT} \tag{2}$$

where B_J is the Brillouin function, defined by:

$$B_J(x) = \frac{2J+1}{2J} ctnh\left(\frac{(2J+1)x}{2J}\right) - \frac{1}{2J} ctnh\left(\frac{x}{2J}\right) \tag{3}$$

for x<<1, and J = ½, we have

$$ctnhx = \frac{1}{x} + \frac{x}{3} - \frac{x^3}{45} \tag{4}$$

and the susceptibility is given by:

$$\frac{M}{B} = \frac{NJ(J+1)g^2\mu_B{}^2}{3kT} = \frac{Np^2\mu_B{}^2\mu_o}{3kT} \tag{5}$$

where p is the number of Bohr magnetons and N is Avogadro's number. Equation (5) is derived based on the assumption that the magnetic moment of atoms is affected by the applied magnetic field only.

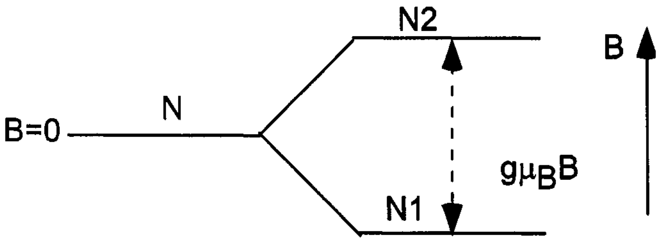

Figure 2-2: Behavior of localized electrons. N is the number of atoms in the absence of magnetic field (B=0). N1 and N2 represent the number of atoms in the lower energy state and higher energy state, respectively, in the presence of magnetic field (B).

Weiss postulated that the magnetic moments of the individual electrons (or atoms) interact with each other resulting in a total magnetic field acting on the magnetic moment of the material as $B = B_e + B_m$, where $B_m = \gamma M$ with γ as the molecular field constant.

$$\chi = \frac{M}{B} = \frac{M}{B_e + B_m} = \frac{C}{T} \tag{6}$$

where $C = \frac{Np^2 \mu_B^2 \mu_0}{3k}$ is the curie constant, solving for M yields

$M = \frac{B_e C}{T - \gamma C}$; therefore, magnetic susceptibility is given by the expression

$$x = \frac{M}{B} = \frac{C}{T - \theta} \tag{7}$$

where $\theta = \gamma C$ is the Weiss constant. Three cases can be identified: $\theta > 0$ where the solid undergoes the transition between the paramagnetic and ferromagnetic phase, $\theta = 0$ corresponds to the simple curie law and $\theta < 0$ applies for solids that undergo the paramagnetic to anti-ferromagnetic transition.

2.2.2 Delocalized (band)electrons

The conduction electrons of a classic metal are itinerant (i.e, they travel through the solid more or less as an electron gas). This is due to very strong interactions between electron wave functions of neighboring atoms in the extended lattice structure[66, 67]. Figure 2.3 illustrates the behavior of band electrons in the presence and absence of magnetic field (B). In the absence of magnetic field (B), the Fermi level of up-spin band matches the Fermi level of down-spin band. When exposed to an external magnetic field (B) only those electrons close to the Fermi-level will respond resulting in a small surplus of one type of spins, as shown in the illustration. This will result in transfer of electrons in order to balance the Fermi level of the band. This effect is a weak form of paramagnetism known as Pauli-paramagnetism. Since the bandwidth is several orders of magnitude greater than kT, Pauli paramagnetism is independent of temperature. The concentration of electrons with magnetic moments parallel to the magnetic field is given by the following equation from Kittel.

$$N_+ = \frac{1}{2}\int_{-\mu}^{\varepsilon_F} f(\varepsilon)d\varepsilon D(\varepsilon + \mu B) \qquad (8)$$

where $f(\varepsilon)$ is the Fermi distribution function and $1/2\,D(\varepsilon + \mu B)$ is the density of orbitals

of one spin orientation with downward shift of energy by -μB. The approximation is written for kT<< ε_F. The concentration of electrons with the magnetic moment anti parallel to the magnetic field is

$$N_- = \frac{1}{2}\int_{-\mu}^{\varepsilon_F} f(\varepsilon)d\varepsilon D(\varepsilon - \mu B) \qquad (9)$$

The magnetization is given by $M = \mu (N_+ - N_-)$ so that the Pauli spin susceptibility is given by the following expression:

$$\chi = \mu_0 \mu_e^2 D(\varepsilon_F) \tag{10}$$

It can be seen from the equation above that the Pauli paramagnetic susceptibility is temperature independent.

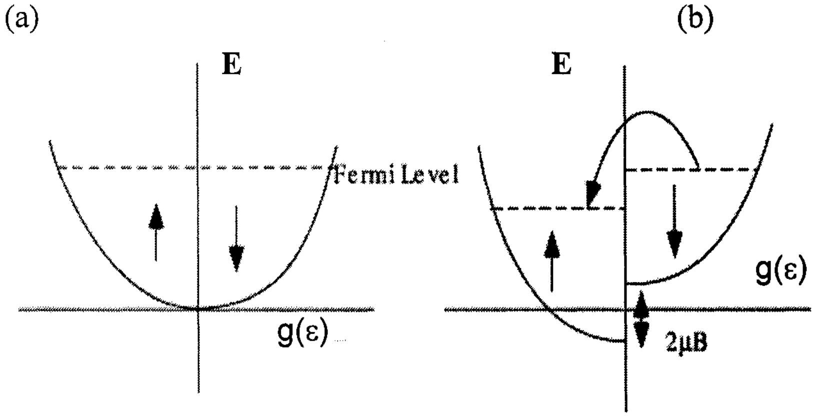

Figure 2-3: Behavior of delocalized electrons in (a) absence of magnetic field (b)in the presence of magnetic field

2.3 Magnetization measurement methods

2.3.1 Induction method

In this method, magnetic measurements can be made in either an AC or DC magnetic field. The DC method and AC method are two different tools for examining magnetic behavior. Both these techniques, however rely on detection coils to measure the magnetic flux variation due to sample magnetization. In DC magnetization method, a sample is magnetized by a static DC field from a superconducting magnet and the resulting change in magnetic flux density is measured. The sample can be subjected to vibration as in vibrating sample magnetometer (VSM) or can be stationary as in Superconducting Quantum Interface Device (SQUID). The output signal from the detection coil corresponding to the variations in flux due to the magnetization of the sample is measured. Alternatively in AC method, the sample is centered within a coil driven with an AC magnetic field which produces a time varying magnetization response detected by the detection coil. Analysis of the response signal can be related to the AC magnetic properties of the sample. Although induction methods provide higher accuracy for smaller samples, it is not suited for in-situ studies of large samples. These methods work well for low temperature magnetization changes in the sample, but high temperature studies using this method are restricted by the complicated circuitry involved.

2.3.2 Force methods:

In the force method of measuring the magnetic susceptibility, the sample's magnetization exerts a force on the sample when placed in a magnetic field. The magnetic energy of the sample changes with applied field and also with position if the magnetic field varies rapidly along a particular co-ordinate. The direction of magnetic moments in the sample will depend upon the type of magnetism; the sample will be pulled or pushed from the field by a force whose magnitude is given by the expression $F_z = \frac{dU}{dZ}$ where U = μB is the internal energy in the presence of magnetic field. It has been found that the apparent gain or loss of mass, i.e., the force, F, exerted on the sample by the magnetic field, B, is

$$F_z = [\Delta m]_{sample} g = 2\chi VB \frac{dB}{dZ} \tag{11}$$

Force methods measure DC susceptibility, the simplest force method used is Guoy balance. The sample is placed in a cylindrical tube which is suspended from the balance and positioned in such a way so that one end of the tube is in zero field while the other end is in a homogenous magnetic field. The force exerted on the sample, which is proportional to the magnetic susceptibility, is measured. The drawbacks of the Guoy balance method include the requirement of large amount of sample for measurement and the dependence of precision on the uniformity of sample packing.

These problems are absent in the Faraday balance which also works on the force principle. The two main sub-types of Faraday systems differ in the manner in which the field gradient is generated. One type uses pole caps on the electromagnet to produce field gradient, therefore both the field and the field gradient increase simultaneously as the current is increased. Sensitivity of the instrument varies as the square of the applied field and the moment sensitivity is linear with the applied field. In the second type, a separate gradient coil is used to produce gradient field and the force on the sample can be made to change sign using a bipolar power supply and the primary uniform field can be varied independent of the gradient coil. This type of configuration is used widely because in the pole cap systems, the magnetic moment sensitivity goes to zero at zero current which limits their application to study permanent moments or hysteresis.

2.4 Summary

A principle advantage of either variant of the Faraday technique is its simplicity and the versatility of the components. The use of a microbalance allows the instrument to be used as a thermogravimetry analyzer (in the absence of magnetic field). In addition, signal to noise ratio is small compared to induction methods because the instrument does not contain sophisticated circuitry and the magnetism of the construction materials is less critical than for induction methods. These features make

Faraday balance ideal for high temperature measurement as it is effectively simpler to incorporate a furnace in the system.

Chapter 3. High temperature Faraday Magnetometer

3.1 Introduction

Magnetic properties of solids have been widely studied using superconducting quantum interface devices (SQUIDs) at temperatures less than 500^{0}C. [38, 55, 69, 70] Many phenomena of interest in transition metal oxides, however, occur at high temperature including catalysis, electronic transport and chemical expansion.[71-74] The extension of SQUID measurements to physically relevant conditions is challenging due to the difficulty of implementing high temperature and atmosphere control within the detection coil of the SQUID. Although Faraday magnetometers have generally fallen out of use for routine magnetic characterization, they are ideally suited for high temperatures and controlled atmosphere when implemented using a modern wide-bore superconducting magnet. Thus they continue to be utilized for magnetization studies of large samples of alloys and inorganic compounds at elevated temperatures.[75]

In this chapter, we describe the design of a high temperature Faraday magnetometer that is sensitive and stable for magnetization and mass change studies in transition metal oxides at temperatures up to 1000^{0}C and in oxygen partial pressures as low as 100 ppm. An essential feature of the design is a compact heating element and surrounding cooling jacket that operates within the narrow bore (3-in) of a modern superconducting solenoid. Also, we demonstrate the operation of the magnetometer using diamagnetic and paramagnetic samples.

3.2 Instrument Design

A schematic of the Faraday magnetometer design is shown in *Figure 3-1*. The main components of the Faraday balance include: 1) A 3-in clear bore superconducting solenoid from American Magnetics Inc, 2) A Cahn D-101 microbalance, and 3) a furnace and cooling jacket assembly. The rated field capacity for the magnetic system is 8 Tesla, with gradients up to 1000 Gauss per inch at the center of the magnet with 100 ppm homogeneity in a 1 cm spherical volume (SV) at the center of the bore. The force on the sample of interest, which is suspended by wire in the SV, is measured using the microbalance, suspended above the magnet system. The D-101 is a force-to-current converter microbalance, consisting of a torque motor and balance beam. The balance is placed on a custom designed stand comprising a goniometry to adjust its angle of inclination.

The essential feature of the design is a high temperature furnace designed to fit in the 3-inch diameter bore of the magnet. The sample is suspended inside an alumina sample tube that is supported by attachments to the balance. Nichrome heating wires are wrapped on the outside of the alumina tube in a non-inductive pattern - *i.e* the wires runs vertically in pairs of opposing current to both minimize and cancel magnetic forces due to electromagnetic coupling to the field. The heating wires are secured on the sample tube using small diameter alumina tubes, cemented in place with Saureisen No. 8 high-temperature cement. The heating element is positioned so that the thermal center coincides with the homogenous region of the magnetic field (SV). The entire furnace is surrounded by insulation material, which is further surrounded by a water-cooled jacket that protects the bore tube of the magnet.

Figure 3-2 shows the cross section of this furnace design and water cooling jacket assembly that fits within the magnet bore. Different insulation materials were used in our attempts to increase the operating temperature of the furnace, the most successful of these involved fiber insulation in conjunction with a vacuum dewar around the heating element. This particular configuration enabled us to reach sample temperature of 1000°C with the temperature outside the cooling jacket not exceeding 55°C. The brass tube serves a dual purpose of supporting the cooling jacket assembly and maintaining the alignment of the furnace with the vertical bore of the magnet. Additional insulation is provided at the end of the furnace element to minimize axial heat loss. Two 0.8 mm thermocouples are used to control and monitor the operation of the furnace: one located just outside the heating element to control DC current to the furnace from a home-built temperature controller, the other located at the external surface of the brass assembly to monitor the temperature of the cooling jacket to insure adequate cooling water. The temperature of the sample inside the alumina sample tube is measured by a third independent thermocouple.

As with traditional thermogravimetry (TG), the magnetic force measurement is prone to several possible random and systematic errors, including vibration, temperature fluctuations around the sample, buoyancy effects, and convective effects inside the sample protection tube. We applied traditional methods of thermogravimetry to limit or correct these errors, including placing the system in a basement laboratory with minimal vibration, establishing the uniformity of the temperature around the sample under gas flow conditions, and measuring and correcting buoyancy and flow effects using blank experiments at zero field.

However, unlike TG, the stray magnetic fields from the superconducting coils introduce systematic errors due to additional torques on the balance beam. Although larger, the effects of the main field are less problematic than that of gradient field, since the value of the main field remains unchanged during most measurements. As such, only a small correctable error in signal gain is introduced. In contrast, the gradient field is ramped up and down during measurements in order to establish changes in magnetization vs. mass. This can alter the baseline from which force changes are established. Since the success of the measurement relies on separating small differences between large numbers, this error must be corrected. In the following, we describe how this error can be reduced by tilting the balance perpendicular to the stray field lines produced by the gradient coil.

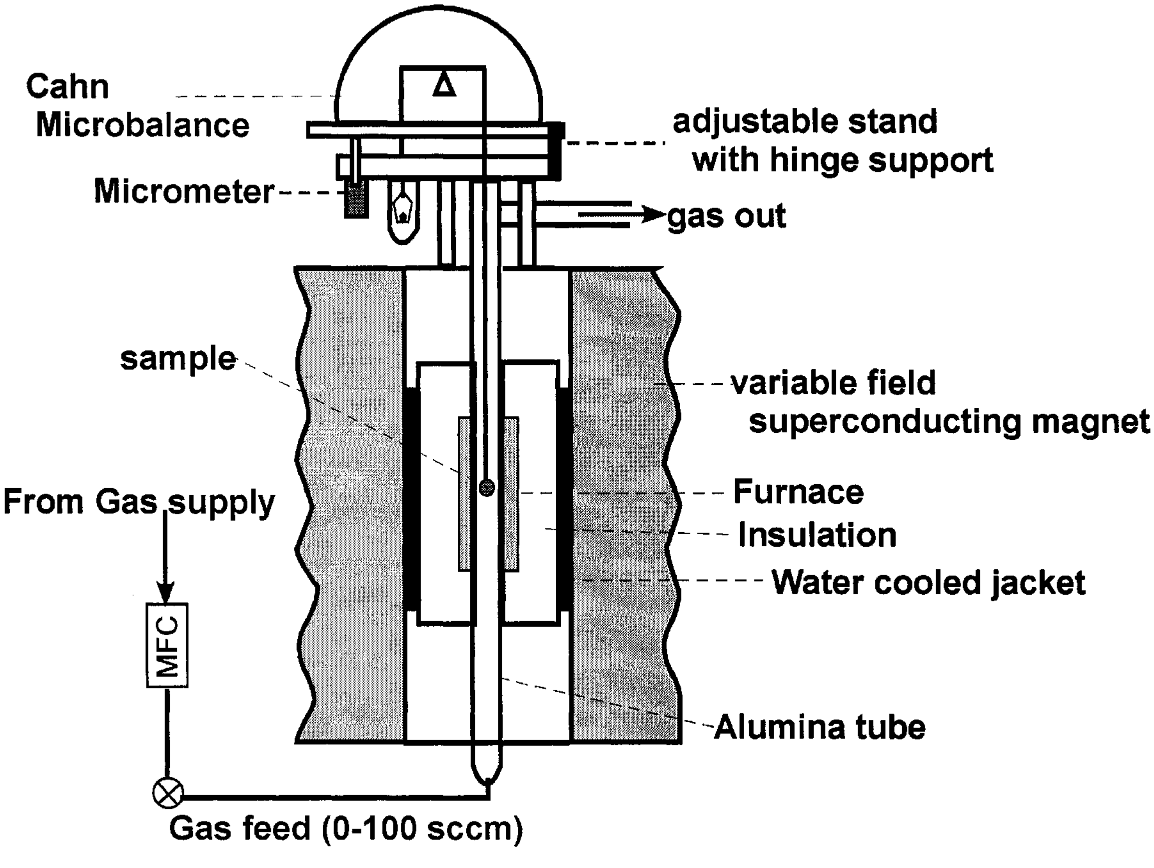

Figure 3-1: Cross-sectional schematic of the instrument assembly

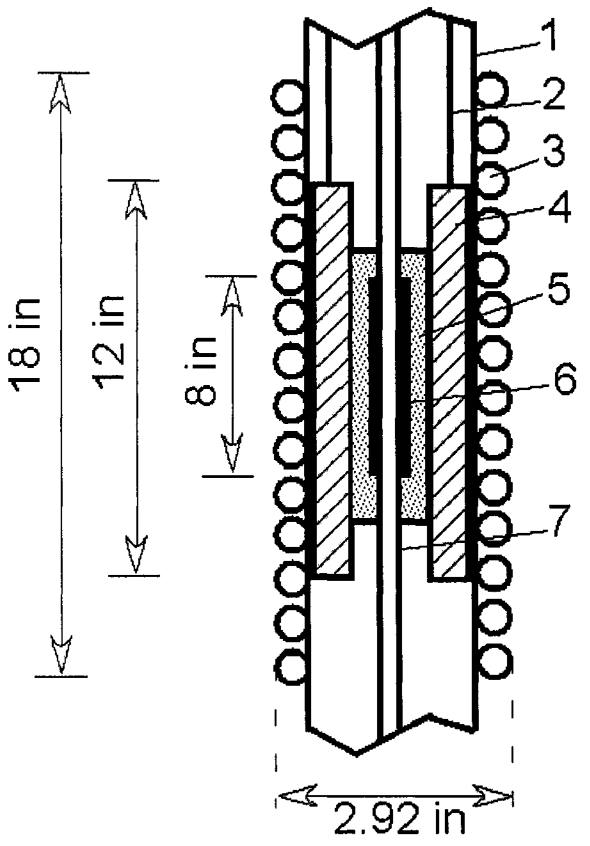

Figure 3-2: Cross section of the furnace–cooling jacket assembly. (1) Brass tube (2.5 in OD) support for water jacket (2) vacuum dewar supporting rod (3) copper tube (3/16 in OD) for circulating water (4) stainless steel vacuum dewar (5) alumina fiber insulation (6) non-inductively wound heating element (7) alumina tube (0.75 in OD)

3.2.1 Tilt correction for stray gradient field

*Figure 3-3*a shows a schematic of the microbalance components. The torque motor, wound vertically with approximately 500 windings, is placed between poles of a permanent magnet of approximately 0.30 Tesla, oriented horizontally. Under normal thermogravimetric operation, the beam is maintained horizontally by dynamically controlling the current in the coil until the torque counters the difference in vertical force acting on the two sides of the beam:

$$(m_s - m_t)gL = NiA\mu_r B_0 \tag{1}$$

where, m_s = sample mass, m_t = tare mass, L = distance between the sample (or tare) and the balance fulcrum (6.6 cm), N = number of turns in the torque motor (500), g = gravitational acceleration (9.8 m/s^2), A = area of the coil (7.6 cm^2), μ_r = average relative permeability of ferromagnetic core of the coil, B_0 = the magnetic field strength of the permanent magnet (0.30 Tesla), and i is the current. The balance signal S, defined as the difference in apparent mass between sample and tare, is calculated from the current by rearranging equation (1):

$$S = \left(\frac{NA\mu_r B_0}{gL}\right) i = (m_s - m_t) \tag{2}$$

When operating as a Faraday balance, the stray field lines of the superconducting magnet overlap the fixed field lines of the permanent magnet in the balance. Since the balance must be mounted off-center from the magnet axis (as shown in Figure 3-1), the stray field is not vertical, but inclined an angle β relative to vertical. Thus the $\sin(\beta)$ component of this field adds to the permanent magnetic field, altering the signal. One way to reduce the effect of this stray field is to tilt the balance at an angle α until the balance beam is perpendicular to the stray field ($\alpha = \beta$). Based on calculated stray field components from American Magnetics, we estimate a value of β to be approximately ~ 6 degrees for the main field and 7.5 degrees for the gradient field.

*Figure 3-3*b illustrates the various forces acting on the balance beam when it is inclined at an angle α with respect to the earth's gravitational field. As discussed in literature, [75]when the balance is inclined, the torque balance in equation (1) must be modified to include the contributions from the balance mass (m_B) and total sample plus tare mass ($m_s + m_t$), which are no longer located vertically above or below the fulcrum. Meanwhile, the magnetic field is modified by the component of stray field perpendicular to angle α, as shown in

*Figure 3-3*c. The net result is:

$$(m_s - m_t)gL\cos\alpha + m_B gd\sin\alpha + (m_s + m_t)gh\sin\alpha = NiA\left(B_0 + B_1\sin(\beta - \alpha)\right) \tag{3}$$

Rearranging to obtain the angle-dependent signal $S(\alpha)$:

$$S(\alpha) = \left(\frac{NA\mu_r B_0}{gL}\right) i = \frac{(m_s - m_t)\cos\alpha + m_B\frac{d}{L}\sin\alpha + (m_s + m_t)\frac{h}{L}\sin\alpha}{1 \pm \frac{B_1}{B_0}\sin(\beta - \alpha)} \tag{4}$$

The sign of the additional stray field contribution in equation (4) depends upon the direction of the gradient field: positive for negative gradient and negative for positive gradient. We can define a systematic error signal $\Delta S(\alpha) = S(\alpha) - S(\alpha)\big|_{B_1 = 0}$, given in the limit of small angle by:

$$\Delta S(\alpha) = \pm\left((m_s - m_t)\cos\alpha + \frac{\alpha}{L}\left(m_B d + (m_s + m_t)h\right)\right)\frac{B_1(\beta - \alpha)}{B_0} \tag{5}$$

Equation (5) shows that $\Delta S(\alpha)$ should vary approximately linearly with α, with a slope approximately proportional to the difference in mass between sample and tare, and go to zero at $\alpha = \beta$. To ascertain if this is true, we determined ΔS experimentally as a function of α by measuring the mass signal of a diamagnetic sample (located outside the magnet) with and without the magnetic field gradient. The balance angle was adjusted by using a micrometer attached to the balance stand.

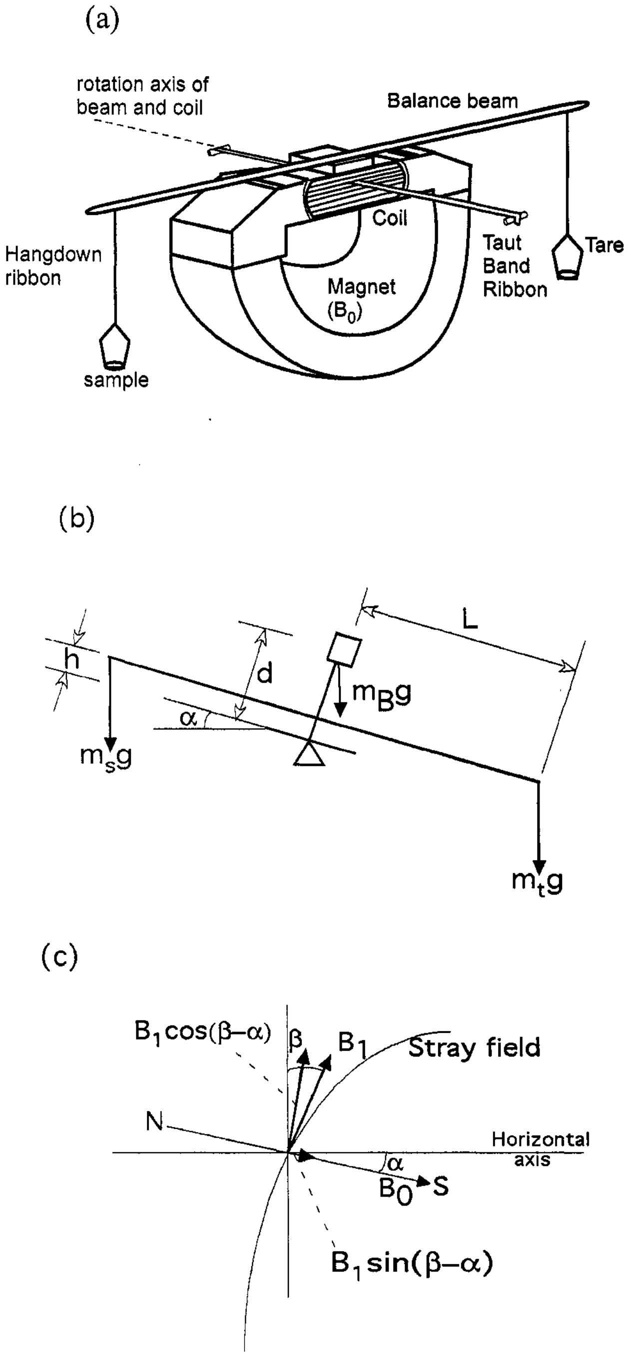

Figure 3-3: (a) Components of the Cahn microbalance. (b) Force diagram for the balance beam inclined at an angle α *.(c) Schematic of stray field component reduction by the introduction of angle* α*.*

*Figure 3-4*a shows the plot of ΔS obtained experimentally for different combinations of m_s and m_t. Agreement is found among scenarios of equivalent values of m_s-m_t (m_s=1g, m_t=0g) and (m_s = 2g, m_t =1g), suggesting that *h/L* and *d/L* are small. In addition, the observed error decreases linearly as angle is increased. However, the measured values do not follow the expected trend from equation (5) for any of the diamagnetic sample masses used. Also, the plot of ΔS at $\alpha = 7.6^{\circ}$ for different sample masses (which should be zero according to equation 5) follows a non-linear trend, as shown in *Figure 3-4*b. One possible explanation for the observed behavior in *Figure 3-4*a could be changes in ferromagnetic ordering within the fixed magnets in the balance. These measurements show that the nullification of stray field effect by mere adjustment of balance angle cannot be accomplished. However, *Figure 3-4*b can be used as an indicator to determine how significant the stray field error contribution would be to the total magnetic force signal for a given sample size. For all the magnetic susceptibility measurements reported below, the balance is set at a angle of $\alpha = 7.6^{\circ}$, and *Figure 3-4* used to determine the degree of systematic error. Future versions of this instrument will include magnetic shielding to more completely minimize this effect.

3.3 Instrument Performance

Transition metal oxides with perovskite structure ($ABO_{3-\delta}$, B = transition metal, A = rare earth cation, δ = oxygen vacancy) exhibit a variety of interesting properties,

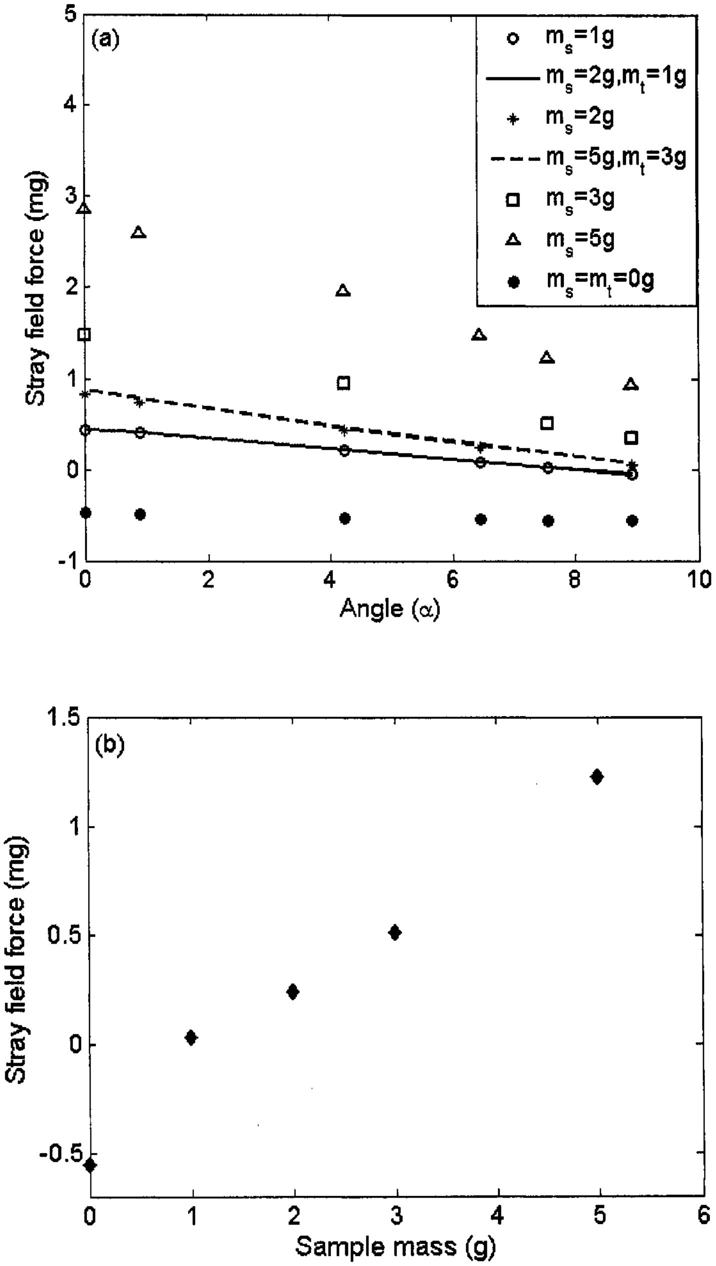

Figure 3-4: (a) Force signal due to stray magnetic field, ΔS for different sample mass (m_s) and tare mass (m_t) combinations (b) ΔS for different values of torque at an angle of 7.6 degrees.

including magnetoresistance, electronic and ionic conductivity, and high-T_C superconductivity.[22, 33, 47, 50, 72] Our research efforts are focused on understanding the catalytic and transport properties of these oxides at high temperatures, and their connection to electronic structure. At high temperatures, the oxygen anions in these oxides become highly mobile, accompanied by electronic and/or crystal structure changes.

The Faraday magnetometer was developed as part of a larger effort to understand these high temperature phenomena from an electronic structure standpoint. In order to establish the sensitivity of the instrument, Lanthanum Strontium Cobalt Oxide, $La_{1-x}Sr_xCoO_{3-\delta}$, of two different composition with $x = 0.7$ (LSC-37) and $x = 0.4$ (LSC-64) along with Aluminum oxide were examined. LSC is a perovskite oxide with rhombohedral symmetry and is paramagnetic at high temperature while aluminum oxide is diamagnetic with nominal stoichiometry that is nominally temperature independent.

*Figure 3-5*a and *Figure 3-5*b show the force signal measured for alumina and LSC 3710, respectively, as a function of temperature using a homogeneous magnetic field of 4 Tesla. Peaks in the plot relative to the baseline indicate the force on the sample measured by the microbalance when a gradient field is applied, henceforth called magnetic force. The magnitude and the direction of magnetic force depend upon the magnetization of the material of interest, and the direction of gradient field respectively.

In alumina at 300^0C, application of positive gradient field introduces a positive magnetic force while the direction of the magnetic force is reversed for a negative gradient field. This is due to the diamagnetic nature of alumina and the orientation of gradient coils in the cryostat. Magnetization of alumina shows no temperature dependence, consistent with diamagnetic behavior in a closed-shell insulator. For LSC-37 at the same temperature, the direction of magnetic force is in the opposite direction than that of alumina, indicating paramagnetism. The magnitude of the force observed for LSC is greater than that of alumina, and shows strong temperature dependence consistent with Curie-Weiss paramagnetism.

The magnetic force for LSC-37 and alumina in *Figure 3-5* is large compared to the baseline error introduced by stray gradient field effects. For alumina at 600^0C, the error is ~5% of the signal, while for LSC-37 it is significantly less. In addition, we found that for diamagnetic samples one can further nullify the error by averaging positive and negative signals obtained by inverting the gradient at the same field strength. *Figure 3-6* shows the magnetic force measured for porous LSC-64 samples at different oxygen partial pressure using a homogeneous magnetic field of 4 Tesla. In this measurement, the magnetic force is measured at 0.21 bar, 0.01 bar and 0.0001 bar oxygen partial pressure at high temperatures. Use of a porous sample ensures that the sample reaches equilibrium with surrounding oxygen atmosphere quickly. Shifts in baseline indicate changes in sample mass due to changes in oxygen content upon reduction/oxidation, while changes in magnetic force with oxygen partial pressure at constant temperature indicate that paramagnetism depends on oxygen content in the sample. Repeatability of the magnetic force is shown at 800^{0}C, where changing the oxygen partial pressure from 100 ppm to air causes the magnetic force to revert to its previously observed values in air. Magnetic susceptibility can be calculated based on this observed magnetic force using the relation:

$$F_z = Sg = \left(\frac{\chi_m B_z}{\mu_0} \frac{dB_z}{dz} \right) \left(\frac{m_0}{MW} \right) \tag{6}$$

where F_z is the magnetic force induced in the z-direction by uniform field (B_z) and field gradient (dB_z/dz), S is the measured magnetic force using microbalance, χ_m is the molar magnetic susceptibility, m_0 is the initial sample mass and MW is the molecular weight of the sample. The magnetic susceptibility of alumina calculated from the force signal in Figure 5a using equation (6) is -0.42×10^{-6}, in reasonable agreement with the literature value [76] of -0.32×10^{-6}. Similarly, the magnetic force on LSC 6410 can be used to obtain the magnetic susceptibility at different oxygen vacancy concentrations.

Figure 3-7 shows the magnetic susceptibility of LSC (6410) calculated using the above procedure. The value of oxygen non-stoichiometry was estimated from the temperature and P_{O2} using a thermodynamic model[49], that will be explained in detail in Chapter 3. The error bars (± 1.5 %) for magnetic susceptibility include the uncompensated stray magnetic force and fluctuations observed in signal at constant

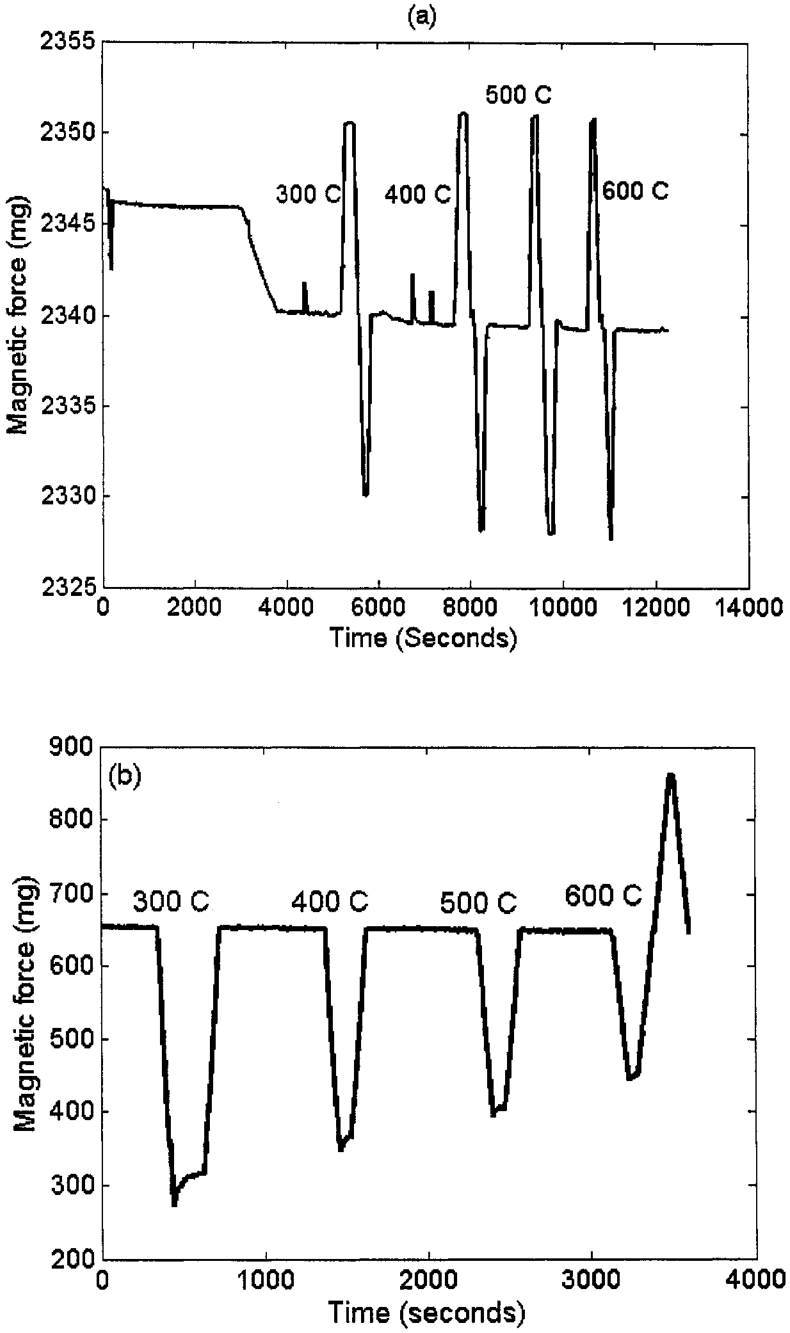

Figure 3-5: Magnetic force signal measured at different temperatures for (a) Alumina (b) LSC 3710

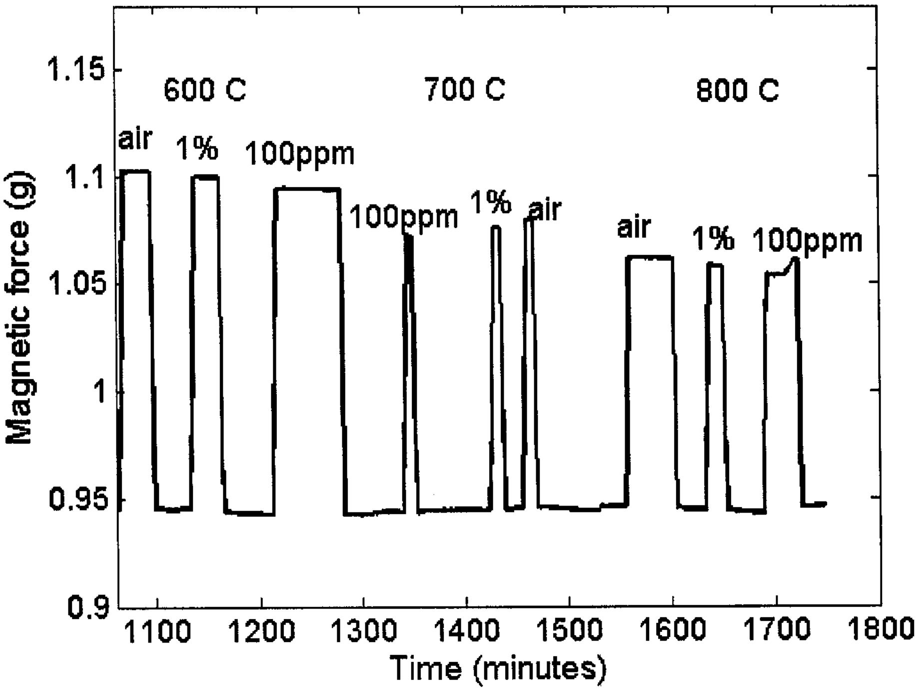

Figure 3-6: Magnetic force signal for LSC 6410 at high temperatures in different oxygen partial pressures

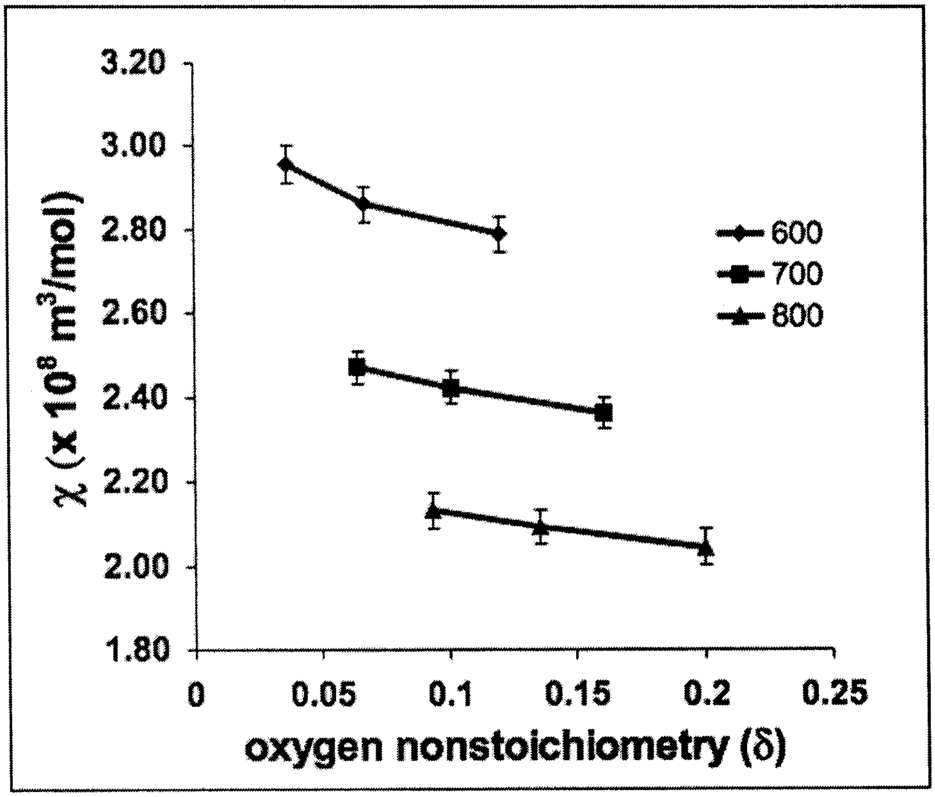

Figure 3-7: Magnetic susceptibility of LSC 6410 as a function of oxygen nonstoichimetry at different temperatures, drawn lines are not fits, but illustrate the magnitude of change.

temperature and magnetic field. This plot is useful in estimating the magnetic susceptibility of an oxide sample at constant oxygen nonstoichiometry.

3.4 Summary

These results show that the high temperature Faraday magnetometer is a promising method for studying the magnetic property changes in transition metal oxides with changes in temperature and oxygen partial pressure. To nullify the stray magnetic field effect completely, mu metal alloy (5% nickel, 15% iron, plus copper and molybdenum) shielding of the balance will be used in future design modifications. Further modification of the instrument will include a vacuum pump that can be used to attain low oxygen partial pressures quickly and will help in transient measurements.

Chapter 4. Oxygen nonstoichiometry: Thermodynamic models

4.1 Introduction

Oxygen nonstoichiometry plays an essential role in determining the properties of electrochemical ceramics, including electrical and ionic transport rates, magnetic behavior, mechanical strain and catalytic properties[23, 77-80]. In the Faraday balance method, magnetic susceptibility is measured as a function of temperature and oxygen partial pressure. However, to understand the effect of temperature and oxidation state on transition metal cations in oxides we need to recast magnetic susceptibility as a function of temperature and oxygen vacancy concentration.

Oxygen nonstoichiometry is usually measured as a function of composition, temperature and oxygen partial pressure, using thermogravimetric analysis (TGA), coulometric titration, or chemical titration[23, 61, 62, 77-82]. Although changes in oxygen nonstoichiometry can be measured experimentally by using the Faraday balance as TGA, the instrument sensitivity is small for measuring small changes in oxygen vacancy concentration. In this chapter, we present thermodynamic models that are widely used in literature for Lanthanum Strontium Iron oxide and Lanthanum Strontium Cobalt oxide.

4.2 Thermodynamic properties of LSF

The oxygen nonstoichiometry, δ, of LSF has been measured over a wide range of conditions by Mizusaki by thermogravimetry [61, 62] and by Yoo with coulometric tiration and conductivity measurements [68]. A plateau in δ occurring at δ = x/2 was observed when oxygen nonstoichiometry was plotted as a function of oxygen partial pressure, as shown in Figure 4-1 for x=0.4 from literature[83]. It should be noted that the plateau also correspond to the oxidation state of +3 for Fe ions in the system. A point defect model that assumes electrons are strongly localized on the Fe ions can explain this plateau. Thus, electrons and holes shift between Fe sites as depicted in Figure 4-2 resulting in hopping type conductivity. In other words, electrons and holes are localized around Fe and can be modeled using point defect approximation of change in oxidation state of Fe ions. The majority charge carriers in the high pressure region are holes while the majority charge carriers in the low pressure region are electrons. Interestingly, a minimum in conductivity is observed when oxygen nonstoichiometry is constant as shown in Figure 4-3, where conductivity undergoes a transition from n-type at low oxygen partial pressures to p-type at higher oxygen partial pressures.

The reaction between oxygen gas and LSF can be expressed in Kroger-vink notation as:

$$\frac{1}{2}O_2(g) + V_O^{\bullet\bullet} + 2Fe_{Fe}^{X} \rightleftharpoons O_O^{X} + 2Fe_{Fe}^{\bullet} \qquad (1)$$

where, in kroger-Vink notation, O_O^x is an oxygen atom, $V_{\ddot{O}}$ is an oxygen vacancy, and $Fe^{\cdot}_{Fe}, Fe'_{Fe}$ are holes and electrons relative to the Fe^{3+} in $LaFeO_3$.

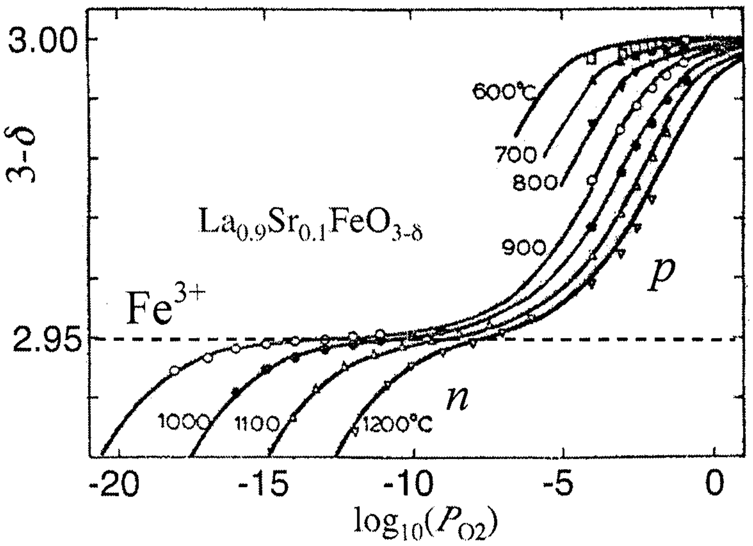

Figure 4-1: Oxygen nonstoichiometry of LSF (x =0.1) from literature[61]

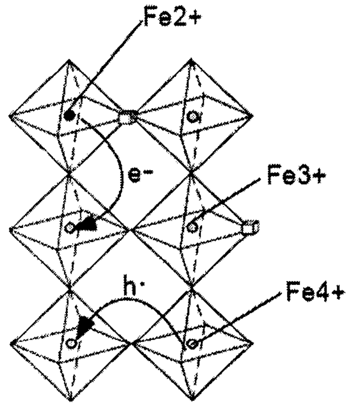

Figure 4-2: Hopping mechanism for conductivity in LSF

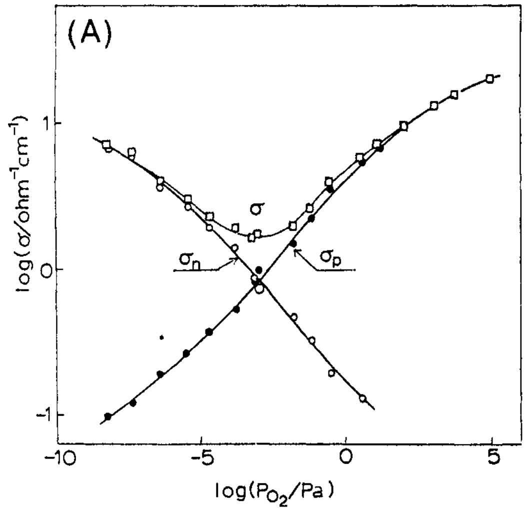

Figure 4-3: Electrical conductivity of LSF(x=0.1) at 1300⁰C from literature[83].

The equilibrium constants for oxidation and ionization reactions, K_{ox} and K_i respectively is given by:

$$K_i = \exp(\frac{\Delta S_i^o}{R})\exp(\frac{\Delta H_i^o}{RT}) \qquad (2)$$

$$K_{ox} = \exp(\frac{\Delta S_{ox}^o}{R})\exp(\frac{\Delta H_{ox}^o}{RT}) \qquad (3)$$

$$K_{OX} = \frac{[O_O^x][Fe_{Fe}^{\cdot}]^2}{P^{1/2}{}_{O2}[V_O^{\cdot\cdot}][Fe_{Fe}^x]^2} \qquad (4)$$

$$K_i = \frac{[Fe_{Fe}^{'}][Fe_{Fe}^{\cdot}]}{[Fe_{Fe}^x]^2} \qquad (5)$$

Oxygen vacancy is modeled as mass-action equilibria among non-interacting localized defects which yield an expression for nonstoichiometry as a function of temperature, oxygen partial pressure and strontium content. With equilibrium constants from equations (4) and (5) along with site and charge neutrality condition, a relationship between oxygen nonstoichiometry and oxygen partial pressure was derived by Mizusaki, as :

$$\frac{(2\delta - x + 1)\delta^{1/2} P_{O2}^{1/4}}{(2\delta - x)^{1/2} P_{O2}^{1/4}} = \frac{K_i}{K_{ox}} \frac{(3-\delta)^{1/2}(x+1-2\delta)}{(2\delta - x)^{1/2} P_{O2}^{1/4}} - K_{ox}^{-1/2} \qquad (6)$$

This model correctly predicts n and p type conductivity at high and low oxygen partial pressure respectively and a plateau in stoichiometry at $\delta = x/2$ as shown in Figure 4-1. This model was used to fit measured nonstoichiometry data and extract enthalpy and entropy thermodynamic values. Although several adaptations of the point defect model presented by Mizusaki have been suggested, this model continues to be considered an accurate description of the thermodynamic relationship between the nonstoichiometry of LSF and the partial pressure of oxygen. This model accurately predicts the nonlinear behavior of oxygen nonstoichiometry with oxygen partial pressure and can be extended to explain the trends observed in electrical properties. Similar formalism has been applied successfully to model the oxygen nonstoichiometry of Cr and Mn doped lanthanum strontium oxides.

4.3 Thermodynamic properties of LSC

The oxygen nonstoichiometry of LSC has been measured over a wide range of conditions by Mizusaki using Thermogravimetry and by Petrov and Lankhorst using Coulometric titration. The value of δ is observed to increase with increasing temperature, increasing strontium content and decreasing partial pressure of oxygen. When oxygen nonstoichiometry values of LSC are plotted vs partial pressure, a plateau, where the concentration of B-site ions of 4+ valance is equal to the concentration of 2+ valance, is not observed (as shown in Figure 4-4). An observed plateau in similar pevoksite oxides, ex: LSF, is thought to indicate that the electrons are localized around the B-site cations. Mizusaki suggests that the lack of a plateau indicates that the electrons are delocalized and that LSC exhibits metallic or semimetallic behavior. Electrical conductivity and Seebeck coefficient measurements of LSC confirmed metallic behavior at high temperatures.

The implications of these observations are 1) the total change in entropy of the system is dominated by configurational entropy of oxygen vacancies 2) changes in entropy due to changes in oxidation state of B-site cation is constant. Oxygen reduction

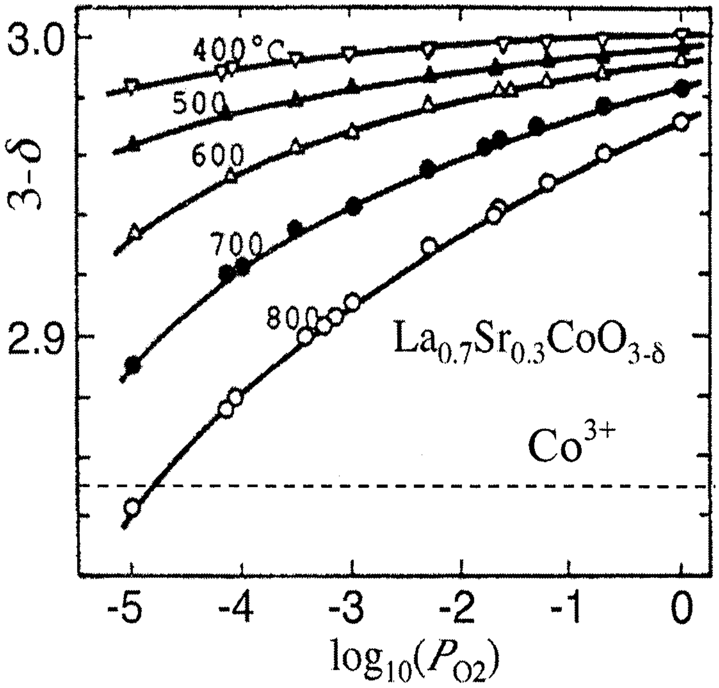

Figure 4-4: oxygen nonstoichiometry behavior of LSC -73 from literature[47].

reaction on a material that obeys a delocalized electron model can be described by the following equation, in Kroger Vink notation:

$$\frac{1}{2}O_2 + V_O^{\bullet\bullet} + 2e' \rightleftarrows O_O^X \quad (7)$$

where $V_O^{\bullet\bullet}$ is an oxygen vacancy (with two net positive charges) and O_O^x is an oxygen atom in a regular oxygen lattice site with a neutral charge. The relationship between deviation of chemical potential from equilibrium, oxygen nonstoichiometry (δ), and oxygen partial pressure as developed by Mizusaki is given by the following equation:

$$\mu_o - \mu_O^0 = \frac{RT}{2}\ln P_{O2} = \Delta h_O^0(x) - a(x)\delta - T\left(\Delta s_O^0 + R\ln\frac{\delta}{3-\delta}\right) \qquad (8)$$

where R is the ideal gas constant, T is the operating temperature, $R\ln\left(\frac{\delta}{3-\delta}\right)$ relates to the configurational entropy change of oxygen vacancies in the system. Mizusaki reports values of these parameters over a range of Strontium content (x), that were extracted from a fit of the measured δ from thermogravimetry experiments to this model.

Lankhorst observed that the enthalpy changes linearly with vacancy concentration, and used different variables to describe the extracted thermodynamic properties. The delocalized electrons in Lankhorst's model, are described as occupying a rigid electron band near the Fermi level, as shown in Figure 4-5 The energy change associated with oxygen vacancy formation/annihilation can be related to change in density of states at the Fermi level, g(ε_F), as expressed in the following equation

$$\mu_{O2} = RT\ln P_{O2} + \mu_{O2}^{0} = E_{ox}(x) - \frac{8\delta - 4x}{g(\varepsilon_F)} - T\left(S_{ox} + 2R\ln\frac{\delta}{3-\delta}\right) \qquad (9)$$

The parameter x is strontium content, Eox (x) is the free energy of oxidation, and Sox is the entropy of oxidation. Lankhorst's thermodynamic model was used to fit the data measured from Coulometric titration measurements to extract thermodynamic parameters, $E_{ox}(x)$, $g(\varepsilon_F)$, and $S_{ox}(x)$. Although different parameters and physical interpretations were used, both models predict similar oxygen nonstoichiometry values as a function of temperature and oxygen partial pressure. However, the deviation from measured oxygen nonstoichiometry values are significant for certain temperature and oxygen partial pressure ranges in these models.

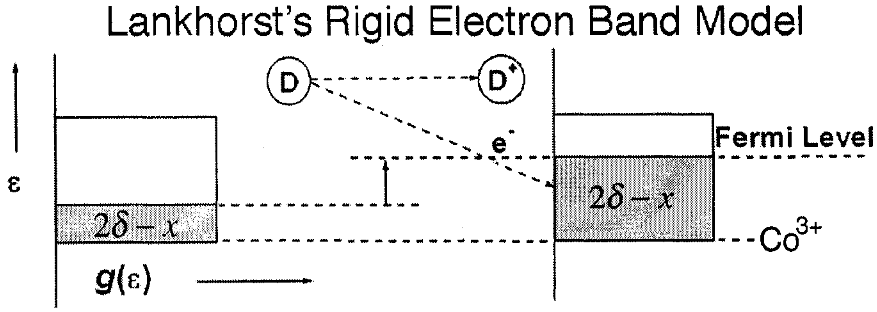

Figure 4-5: Rigid electron band model, as developed by Lankhorst to explain oxygen nonstoichiometry behavior as a function of temperature and oxygen partial pressure.

To get an accurate value for oxygen nonstoichiometry over the wide range of temperature and oxygen partial pressure, we used a modification of Lankhorst's rigid band model. This model was used to interpolate previously measured oxygen nonstoichiometry properties of LSC. In Lankhorst's original model, it is assumed that the density of states, g(ε_F), is constant, i.e., a square rigid electron band, as shown in Figure 4.5. In our modification of this model, we hypothesize that changes in the stoichiometry are significant enough that band curvature may be important, such that the density of states vary with electron occupation changes, as showin in Fig xx. We have modeled this effect to first order by allowing $g(\varepsilon) = g_o(\varepsilon_o) + g_1(\varepsilon_1)(\varepsilon - \varepsilon_0)$, where $g_o(\varepsilon_o)$ is the density of states evaluated at electron energy $\varepsilon_o, g_1(\varepsilon_o)$ is the first derivative of g(ε) and ε_o is the Fermi energy when the electron occupation number n_e (as defined by Lankhorst) is given by $n_e = 2\delta - x$. This assumption results in the following implicit expression for δ(T, Po_2):

$$\mu^o_{O2}(T) + RT \ln P_{O2} = E_{ox} - TS_{ox} - 2RT \ln\left(\frac{\delta}{3-\delta}\right) - 4\left(\frac{n_e}{g_o(\varepsilon_o)} - \frac{n_e{}^2 g_1(\varepsilon_o)}{g_o{}^3(\varepsilon_o)}\right) \quad (10)$$

Figure 4-6 through Figure 4-7 show fits to measured oxygen nonstoichiometry as a function of temperature and oxygen partial pressure using this modification (for x=0.2, 0.4 and 0.7 respectively) and the thermodynamic parameters used to obtain the fit are shown in Table 1

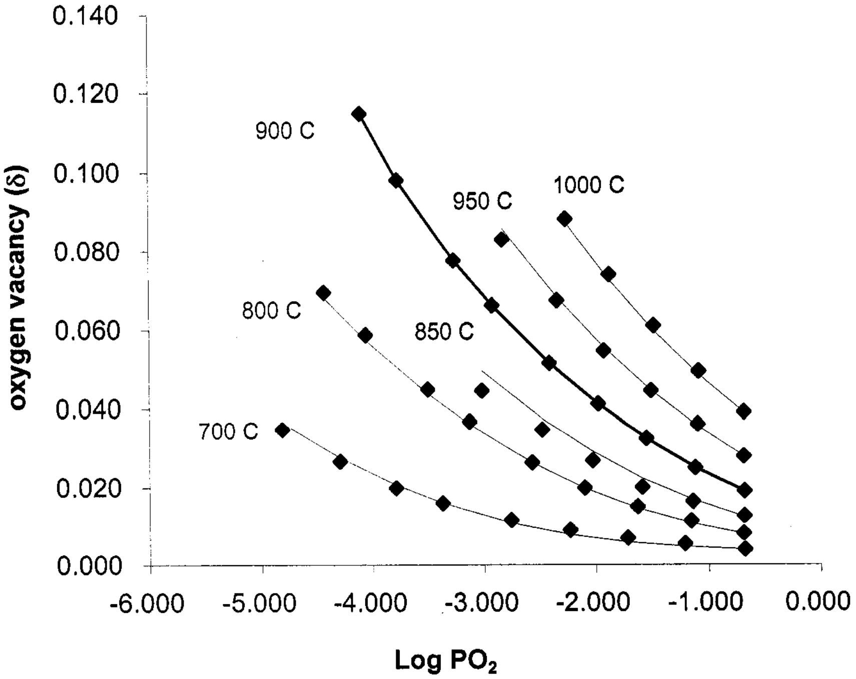

Figure 4-6: Oxygen nonstoichiometry values for LSC (x=0.2) at different temperatures. Drawn lines are fit to equation(10)

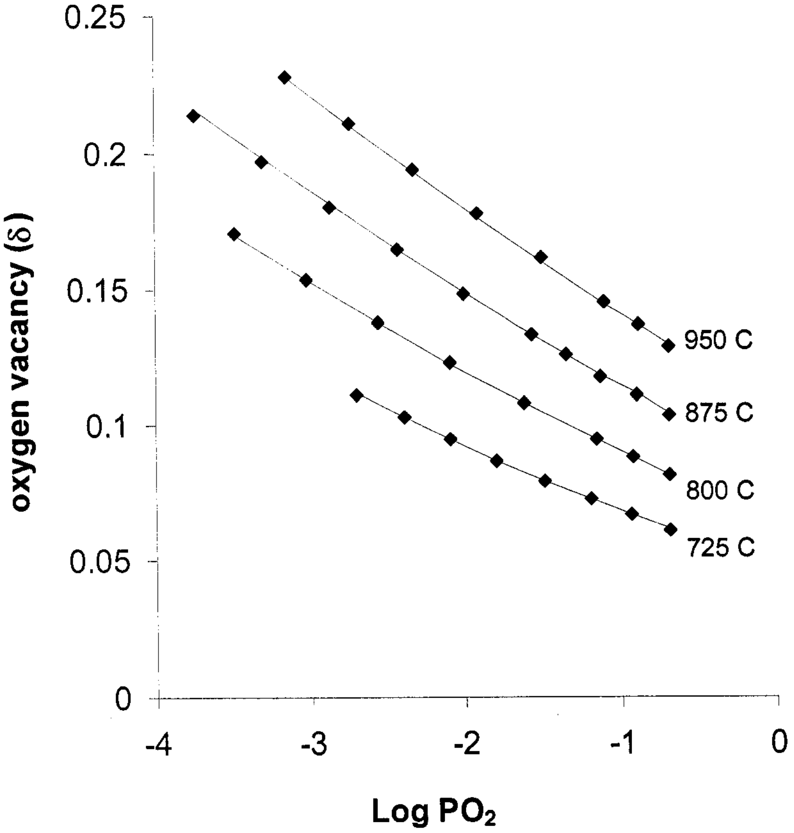

Figure 4-7: oxygen nonstoichiometry values for LSC (x=0.4) at different temperatures.Drawn lines are fit to equation(10)

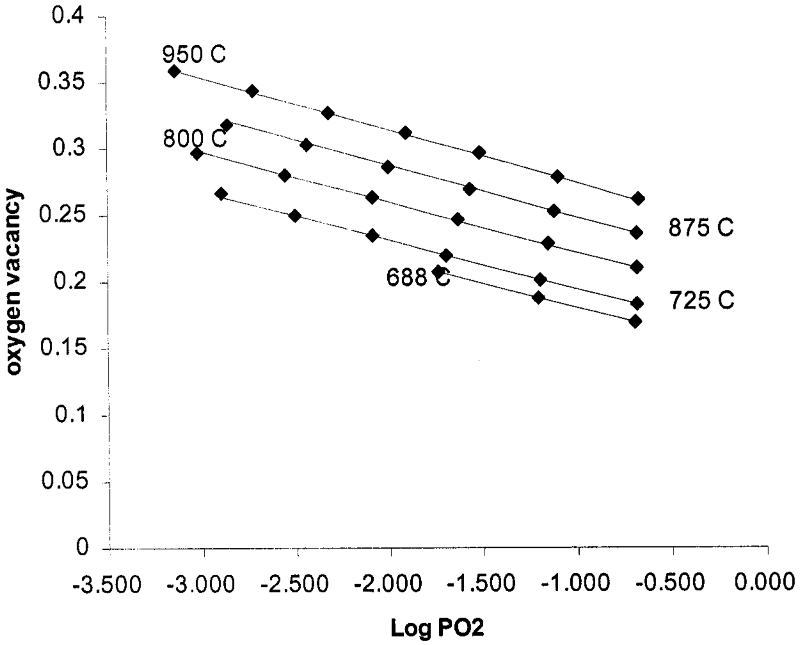

Figure 4-8: oxygen nonstoichiometry values for LSC (x=0.7) at different temperatures.Drawn lines are fit to equation(10)

Table 4-1: Fitting parameters used in equation to obtain the fits for various Strontium composition[84, 85]

	x =0.2	x =0.4	x =0.7
Eox, kJ/mol	-335.19	-288.57	-246.61
Sox, J/mol.K	69.10	92.88	137.04
$g_o(\varepsilon_f)$, x 10^{-5} $(J/mol)^{-1}$	3.06	1.86	1.35
$g_1(\varepsilon_f)$ x 10^{-10} $(J/mol)^{-2}$	67.89	1.30	-1.83

4.4 Summary

The point defect model for LSF can be used to accurately predict oxygen nonstoichiometry over wide range of temperature and oxygen partial pressure. We modified an existing thermodynamic model for LSC, using an additional parameter to incorporate the effect of band curvature. We generally found this model to fit the data better than previous models over the range of available measured values of oxygen nonstoichiometry. Although extremely successful in predicting oxygen nonstoichiometry values over a wide range of temperature and oxygen partial pressure, the physical significance of the parameters obtained from the fit is not clear. The value of density of states obtained is similar to the values obtained from original model. However, it is difficult to separate the effect of temperature on thermodynamic parameters, E_{ox} and S_{ox}. It is clear that the changes in oxygen nonstoichiometry are very closely related to nature of electrons in the system.

Chapter 5. High temperature magnetic property of LSF

5.1 Introduction

The unique electrical properties of LSF are closely related to the defect chemistry involved. Upon the substitution of strontium for lanthanum, the difference in ionic charge between Sr^{2+} and La^{3+} must be compensated by creation of oxygen vacancies and/or change of oxidation state of iron. A point defect model, proposed by Mizusaki [61], (as discussed in Chapter 4) has been widely used to interpret oxygen vacancy behavior as a function of temperature and oxygen partial pressure in these oxides. Recent calorimetric studies have measured the energetics involved in the oxygen incorporation reaction. It is confirmed that the energy for oxygen incorporation, within experimental errors, is independent of oxygen vacancy concentration in the system[79].

Besides being an ideal candidate for high temperature electrochemical applications owing to its high electronic and ionic conductivity, LSF is an excellent material for understanding high temperature magnetic property of a localized system. Previous studies in LSF have shown that magnetic interactions are strongly a function of oxygen vacancy concentration in the system[86-88]. Magnetization measurement on $La_{0.6}Sr_{0.4}FeO_{3-\delta}$ showed that samples with low oxygen nonstoichiometry have a magnetic ordering temperature in the range of 300K – 325 K while those with 12%

oxygen vacancies have a magnetic ordering temperature of 800K and higher[88, 89]. The oxidation state of iron is closely related to the nature of magnetic interaction in iron oxides. For instance, $LaFeO_3$, (Fe in +3 oxidation state) showed spin ordered anti-ferromagnetic structure while the interaction is reported as ferromagnetic in $SrFeO_3$ (Fe in +4 oxidation state)[39, 90]. Neel temperature (defined as the temperature of antiferromagnetic to paramagnetic transition) has been found to be dependent on Sr composition in LSF[39, 88, 90, 91].

In many of these earlier studies, the measurements were based on samples quenched under different temperature and oxygen partial pressures. Recent measurements in similar perovskite oxides have shown that these materials undergo chemical expansion (in addition to thermal expansion) which is strongly a function of oxygen vacancy concentration[78, 85]. Earlier studies have confirmed a strong correlation between bond length fluctuations and magnetic interactions in these types of systems. In order to understand the effects of oxygen vacancies on magnetic interactions at high temperature, it is important to measure magnetic property not only as a function of temperature but also as a function of oxygen partial pressure. The purpose of the present work is to measure high temperature magnetic property of LSF as a function of temperature and oxygen partial pressure. The oxygen vacancy concentrations reported in this chapter were calculated using Mizusaki's point defect model, discussed in Chapter 4.

5.2 Experimental details

Commercially available powders of $La_{0.8}Sr_{0.2}FeO_{3-\delta}$ (LSF-82), and $La_{0.6}Sr_{0.4}FeO_{3-\delta}$ (LSF-64) from Praxair, Inc. were sintered into porous bars using cornstarch as a pore former. The powders were pressed into 45mmx5mmx5mm bars using a uniaxial press with a pressure of approximately 4500psi. The bars were heated at a rate of 1°C/min to 1250°C, held at that temperature for 6 hours in air, and cooled down at 1 °C/min to room temperature. The porosity of the sintered samples were found to be in the range of 35-45%, measured using Archimedes method. The use of a porous sample facilitates equilibrium between gas and solid P_{O2} at lower temperatures. The bar was cut into segments approximately 5 mm in length, and notched to accommodate a suspension wire.

High temperature magnetization measurements were carried out using high temperature Faraday balance, described in Chapter 3. Oxygen vacancy at temperatures and oxygen partial pressures of interest, were calculated using point defect model for LSF as detailed in Chapter 4.

5.3 Results and discussion

Figure 5-1 shows the magnetic susceptibility of LSF 82 as a function of electron occupancy, as defined by Lankhorst, at three different temperatures. The electron occupancy in LSF corresponds to the oxidation state of iron. Electron occupancy of zero corresponds to Fe^{3+} and negative electron occupancy indicates a mixture of Fe^{3+} and Fe^{4+} in the material. The values of oxygen nonstoichiometry used to calculate electron occupancy are based on thermodynamic model discussed in Chapter 4.

Figure 5-2 shows the magnetization plot for LSF 6410 in similar temperature and oxygen partial pressure range. In both these compositions, magnetic susceptibility show strong temperature dependence, an indication that magnetic susceptibility follows Curie-Weiss behavior. Magnetic susceptibility increases with increasing oxygen vacancy concentration suggesting that oxidation/reduction in these materials involves localized energy states.

LSF is p-type in the range of Po_2 used in the present study, hence the charge neutrality requirement in the lattice yields

$$-[Fe_{Fe}^{\bullet}] = n_e = 2[V_O^{\bullet\bullet}] - [Sr_{La}^{'}] \tag{3}$$

where n_e is the electron occupancy number. In equation (3), we have assumed that the concentration of Fe^{2+} is negligible. In the range of temperature used for the current measurement, the spin states of iron are high spin. The number of unpaired spins in Fe^{3+} and Fe^{4+} are 4 and 5, respectively. With increase in electron occupancy, Fe changes oxidation state from 4+ to 3+ and we expect an increase in magnetic susceptibility (as electron occupancy approaches zero). However, the trends observed in Figure 5-1 and Figure 5-2 is opposite the expected trend. One possible explanation for this observed trend is that changes in oxygen vacancy concentration of the sample results in changes in oxygen vacancy concentration of the sample results in changes in magnetic interaction .

Oxygen vacancy changes in the system can cause shifts in bond length that contribute to additional expansion in the lattice. The Curie-Weiss law discussed in Chapter 2: $\chi_{CW} = \frac{C}{(T-\theta)}$ can be rearranged in the form:

$$\chi_{CW} = \frac{1}{\left(\frac{T}{C} - \lambda\right)} \qquad (4)$$

where the relation between average molecular field and Weiss constant, $\theta = \lambda C$ is used. C is the Curie constant given by $C = \frac{p^2 \mu_0 \mu_B^2 N}{3k}$. In equation (4), the average molecular field (λ) is related to the magnetic interaction in samples. The Curie constant is proportional to the number of Bohr magnetons (p), which is related to the total spin number (S) of electrons:

$$p = g\sqrt{S(S+1)} \qquad (5)$$

where g is the spectroscopic splitting factor (≈2). This way of representing Curie-Weiss law enables us to separate the magnetic interaction (λ) effects and temperature effects on paramagnetic susceptibility.

In order to have an expression to predict paramagnetic susceptibility as a function of electron occupancy, we use the HS configuration for Fe^{3+} and Fe^{4+}. Based on the condition that when electron occupation is zero, the total spin number (S) must equal to the value for Fe^{3+} (= 5/2), we obtain:

$$S = \frac{(5 + 2\delta - x)}{2} \tag{6}$$

Therefore, we get an expression for paramagnetic susceptibility explicitly dependent on electron occupancy as:

$$\chi_{CW} = \frac{1}{\left(\dfrac{3kT}{g^2 \mu_B^2 S(S+1) N \mu_0} - \lambda \right)} \tag{7}$$

where S is given by equation (6). Equation (7) can be used to predict theoretical value of magnetic susceptibility a function of electron occupancy. We find that the theoretical prediction matches experimental behavior closely, as shown by drawn lines in Figure 5-1 and Figure 5-3. Figure 5-3 (a) and (b) shows the values of λ used to obtain the fit, and corresponding ordering temperature (θ) as a function of oxygen nonstoichiometry respectively. Figure 5-4 shows a plot of magnetic interaction parameter (λ) as a function of oxygen vacancy concentration in LSF -64.

Magnetic interactions in LSF are presumed to arise through a super exchange between 3d transition metal electrons via oxygen orbitals. At a particular temperature, an increase in oxygen vacancy affects this interaction by significantly altering the bond angle. This would lead to an increase in ordering temperatures with oxygen vacancies as shown in Figure 5-2(b). The estimated value of θ is reasonably close to the typical ordering temperature values found in literature[39, 64, 65]. Figure 5-5 shows a plot of parameter λ as a function of oxygen vacancies in both the compositions studied. Interestingly, when data from both the compositions are compared, λ appears to scale with electron occupancy, rather than oxygen vacancy concentration.

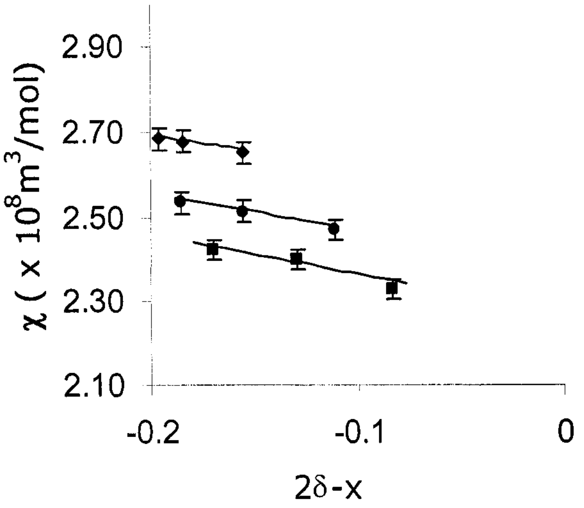

Figure 5-1: Magnetic susceptibility of LSF 8210 as a function of electron occupancy at 709 C (◆), 820 C (●) and 903 C (■). Drawn lines represent fitting from equation (4)

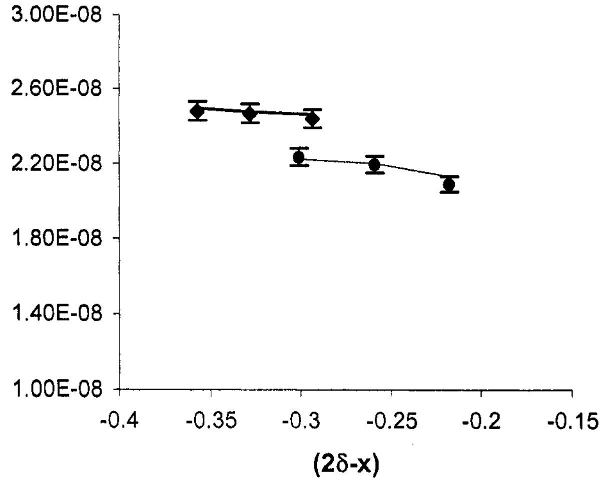

Figure 5-2: Magnetic susceptibility of LSF 6410 as a function of electron occupancy at 709 C (◆) and 825 C (●). Drawn lines represent fitting from equation (4)

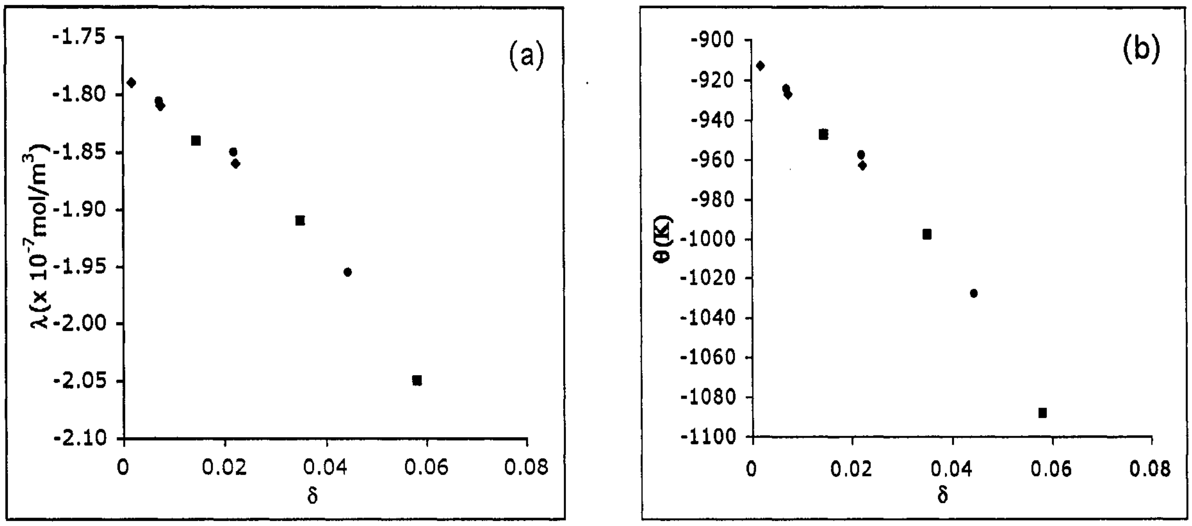

Figure 5-3: (a) Magnetic interaction parameter, λ for LSF at different temperatures as a function of oxygen non-stoichiometry. (b) Ordering temperature, θ corresponding to lambda values as a function of nonstoichiometry.

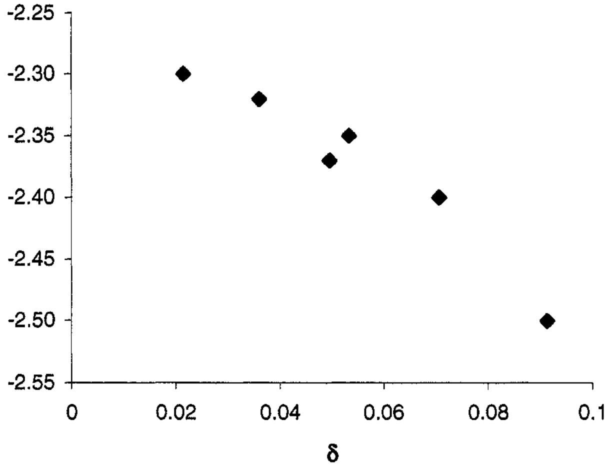

Figure 5-4: Magnetic interaction parameter, λ for LSF-64 at different temperatures as a function of oxygen nonstoichiometry.

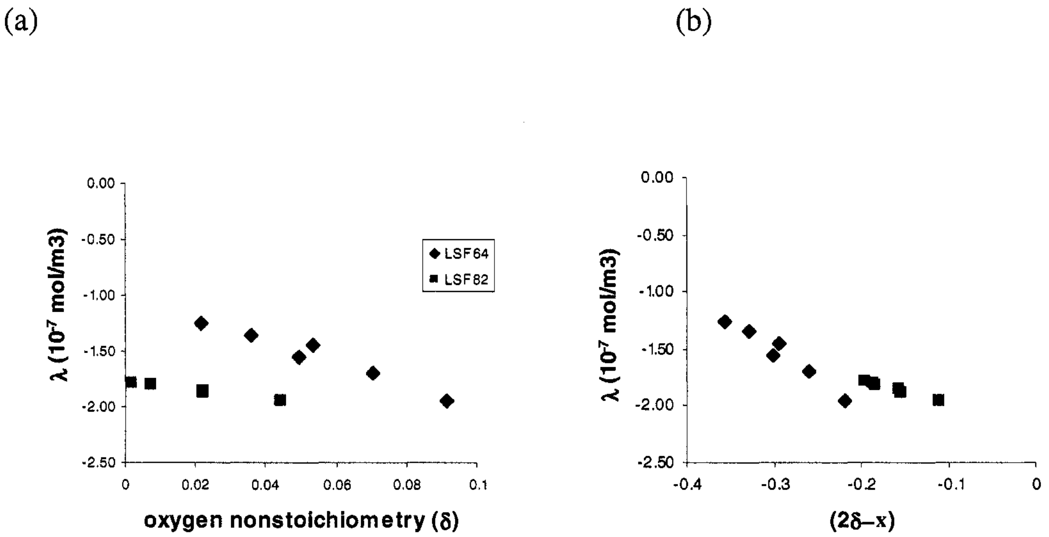

Figure 5-5: Parameter, λ, as a function of (a) oxygen nonstoichiometry and (b) electron occupancy.

5.4 Summary

High temperature magnetic behavior of LSF is consistent with the expected behavior from localized electronic system. These measurements also show a strong correlation between the oxygen vacancy concentration and the type of magnetic interaction. This is consistent with earlier low temperature studies in LSF systems, where a correlation between oxygen vacancy concentration and magnetic ordering temperature has been found.

We found, by using an adjustable parameter λ , that theoretically predicted values of magnetic susceptibility match closely with that of experimental trends. This parameter appears to show stronger trend with oxidation state of iron (electron occupancy), rather than oxygen vacancy concentration. Magnetic interaction in LSF is found to be closely correlated with the oxidation state of iron.

Chapter 6. High temperature magnetic properties of LSC

6.1 Introduction

LSC of varying strontium composition is used to study the correlation between electronic structure and defect concentration at high temperatures as a function of oxygen partial pressure. Also, transport (electrical conductivity) measurement along with calorimetric studies are included in this work which compliments the magnetic measurement to correlate observed properties with electronic structure and its variation with defect concentration. Oxygen nonstoichiometry of the samples was calculated based on the thermodynamic model discussed in the previous section. In this chapter, we discuss the observed magnetic and electrical properties at high temperature and compare to existing theories of electronic structure.

6.2 Experimental details

6.2.1 Sample preparation and characterization

Commercially available powders of $La_{0.8}Sr_{0.2}CoO_{3-\delta}$ (LSC-82), $La_{0.6}Sr_{0.4}CoO_{3-\delta}$ (LSC-64), and $La_{0.3}Sr_{0.7}CoO_{3-\delta}$ (LSC-37) from Praxair, Inc. were sintered into porous bars using cornstarch as a pore former. The powders were pressed into 45mmx5mmx5mm bars using a uniaxial press with a pressure of approximately

4500psi. The bars were heated at a rate of 1°C/min to 1200°C, held at that temperature for 6 hours in air, and cooled down at 1 °C/min to room temperature. The porosity of the sintered samples was found to be in the range of 35-45%, measured using Archimedes method. The use of a porous sample facilitates equilibrium between gas and solid P_{O2} at lower temperatures. The bar was cut into segments approximately 5 mm in length, and notched to accommodate a suspension wire. The porous samples used in the study were confirmed as single-phase perovskite structure by room temperature X-ray diffraction.

The LSC samples used for magnetic measurements were characterized using XRD to test whether the samples are in single phase. Both in-situ and ex-situ measurements were carried out to understand the structural transitions, if any, as a function of temperature and oxygen partial pressure.

Figure 6-1 and Figure 6-2 show XRD pattern of as-sintered LSC 64 and LSC 64 quenched at 900 ^{0}C and 100ppm of oxygen in nitrogen. The peak positions indicate that the samples retain the perovskite structure and do not indicate any phase instability in the samples used for the measurement. However, recent in-situ measurement on LSC 3710 and LSC 8210 samples suggest that depending on the sample preparation conditions, there might be additional phases such as CoO or Co_3O_4. Similar phase separation has been observed in samples used for chemical expansion measurements purchased from SCI engineered materials. Such instabilities have not been observed for the samples from Praxair that are used in this work.

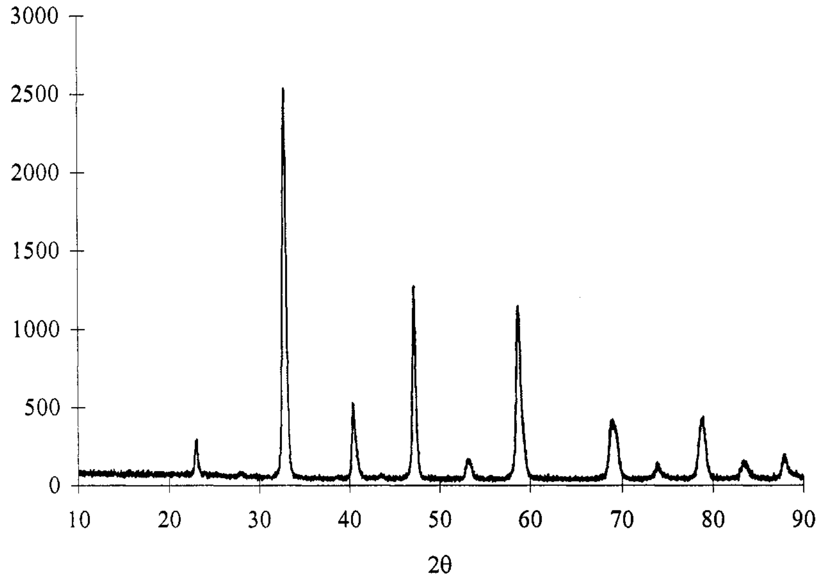

Figure 6-1: XRD pattern of as-sintered LSC 6410

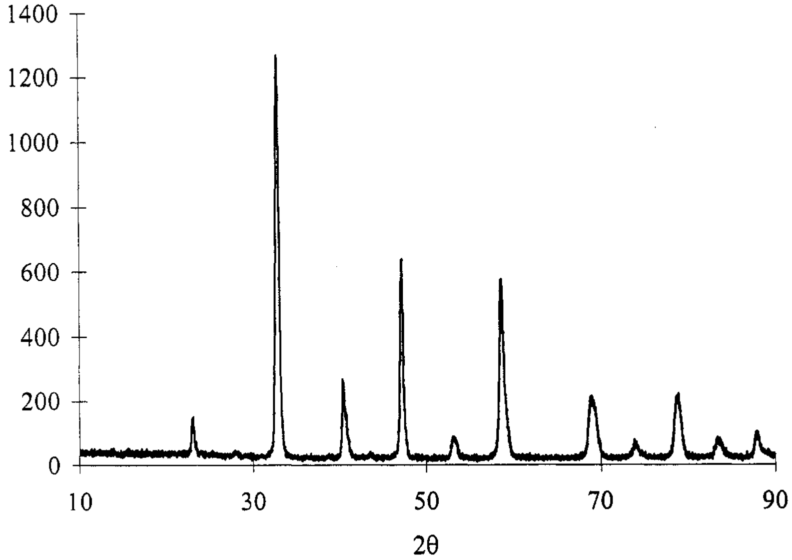

Figure 6-2: XRD pattern of LSC 6410 quenched at 900 °C and 100 ppm ($\delta = 0.27$)

Low temperature magnetic measurements (from 5K up to 350K) were carried out using semiconducting quantum interface device (SQUID). LSC is ferromagnetic at low temperatures, ferromagnets exhibit history dependent behavior i.e. the value of magnetization is dependent on the sequence of magnetic field changes and temperature changes that were involved in getting the sample to the conditions in which it was measured. This type of behavior can be observed by zero field cooled (ZFC) and field cooled (FC) set of measurements.

In this technique, the sample is cooled to the lowest measurement temperature in zero magnetic field.. Once the temperature is stabilized, magnetic field is applied and magnetization is measured as a function of temperature up to the highest temperature desired, this is the ZFC part. This is followed by cooling the sample in this same field to the lowest temperature, and again measuring the magnetization. This is the FC part. These measurements show temperature range over which the ferromagnetic system becomes irreversible.

Magnetic ordering temperature as a function of oxygen vacancy concentration in the sample is measured using quenched samples. High temperature magnetic measurements (between 700^0C and 920^0C) as a function of oxygen partial pressure were carried out using high temperature Faraday balance.

6.3 Results and Discussion

6.3.1 Low temperature magnetization

ZFC/FC measurements were done to determine whether LSC is ferromagnetic at low temperatures. Figure 6-3 shows low temperature magnetization measurement of LSC-64. The ZFC/FC curves shows the range of temperature over which the ferromagnetic material becomes irreversible. LSC-64 and other samples of LSC (based on similar low temperature magnetic measurements) have been found to be ferromagnetic. The local paramagnetic moments order at 198K, 242K and 221K, respectively, for LSC-82, LSC-64 and LSC-37.

It is understood that magnetic ordering temperature is function of strontium composition, however, it is not clearly understood how the ordering temperature varies with oxygen vacancy changes. In order to estimate the amount of variation of θ, low temperature magnetization measurements were carried out on samples quenched at different conditions. LSC -64 sintered samples were quenched at different temperatures and oxygen partial pressures to freeze in the oxygen vacancies. Although all the samples showed identical ferromagnetic behavior, the value of ordering temperature decreased with increase in oxygen nonstoichiometry. Figure 6-4 shows a plot of ordering temperature (θ) as a function of oxygen nonstoichiometry in the sample.

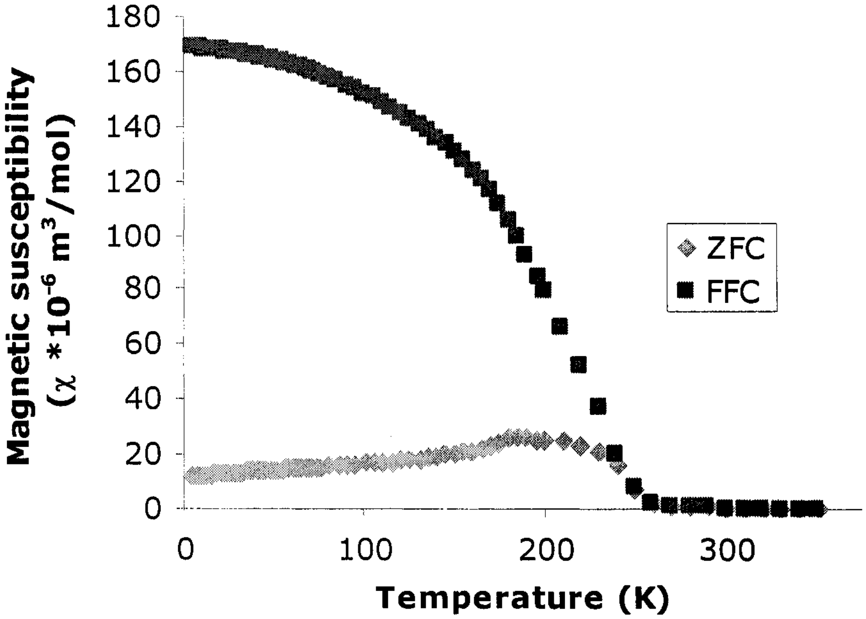

Figure 6-3: Low temperature magnetization (FC and ZFC) for LSC-64

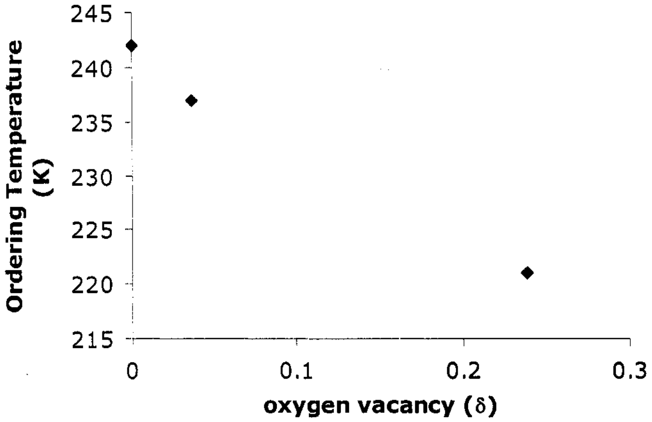

Figure 6-4: Plot of ordering temperature as a function of oxygen vacancy concentration

6.3.2 High temperature magnetization

High temperature magnetic force measurements were carried out using a Faraday magnetometer. Measurements were made at a uniform magnetic field of 5 Tesla and a gradient field of 1000 Gauss/inch. Oxygen partial pressure in the instrument was controlled using blended gases of oxygen in nitrogen. The flow rate of the feed gas was maintained at 100 sccm by a mass flow controller. Electrical conductivity of LSC-82 and LSC-64 were measured using the AC four probe technique at low frequencies, and corrected for porosity.

Magnetic susceptibility measurements were made as a function of temperature and oxygen partial pressure. To recast our measurement $\chi(T, P_{O2})$ in the form $\chi(T, \delta)$, we used a modified version of Lankhorst's rigid band model, discussed in chapter 4 to interpolate previously measured oxygen nonstoichiometry properties of $La_{1-x}Sr_xCoO_{3-\delta}$[49, 78]. This modification adds a parameter that improves overall fit, and for our purposes here should be thought of simply as an empirical interpolation of the data. Accuracy in reproducing $\delta(T, P_{O2})$ is better than ±10% over the range of conditions studied.

Figure 6-5 shows a plot of magnetic susceptibility versus Cobalt oxidation state, expressed in terms of the "electron occupation number," $n_e = 2\delta\text{-}x$, as defined by Lankhorst [49]. Increasingly negative values of n_e represent positive deviations of the Co oxidation state from its formal valance of Co^{3+}. Assuming an intermediate spin configuration with delocalized Co^{3d}-O^{2p} σ^* band, n_e also represents the deviation of the band occupancy from half-filled.

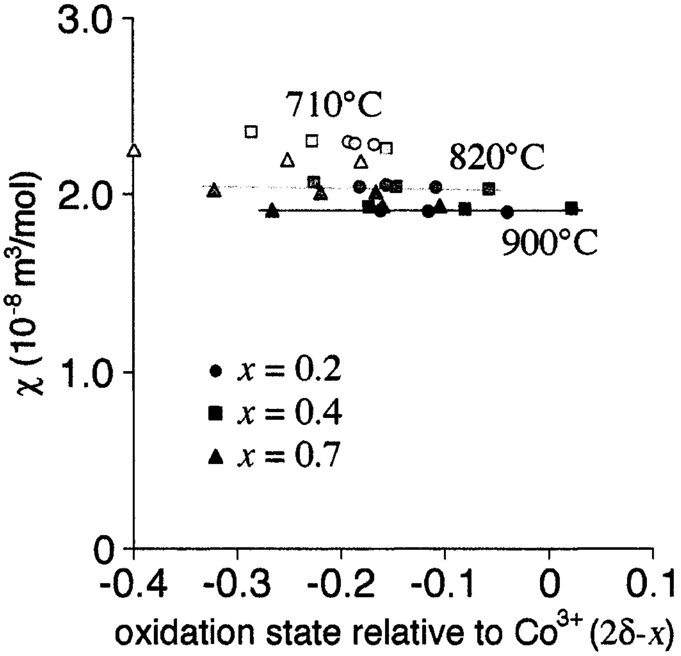

Figure 6-5: High temperature magnetic susceptibility of LSC as a function of electron occupancy, Sr content (x) (symbols), and temperature (color/grayscale). Lines are merely an indication of the trend

The data in *Figure 6-5* reveal that as temperature is increased, magnetic susceptibility of LSC collapses to a nearly universal dependence on oxidation state, regardless of Sr doping. At the highest temperatures, magnetic susceptibility is independent of oxidation state, consistent with entirely delocalized valence electrons. As the temperature is lowered, some dependence of χ on electron occupancy appears, possibly suggesting the onset of localization effects.

Figure 6-6 shows a plot of electrical resistivity as a function of oxygen nonstoichiometry (δ), Sr content (x), and temperature. In addition to our measurements at $x = 0.2$ and $x = 0.4$, we have also included previously published measurements at $x = 0.3$ [50]and $x = 0.7$. [23] The data show that materials of different Sr content exhibit remarkable similarities in the way resistivity scales with δ and T. At a given value of δ, resistivity increases modestly with temperature (consistent with metallic behavior), while at a given temperature resistivity scales strongly (and nonlinearly) with oxygen vacancy concentration.

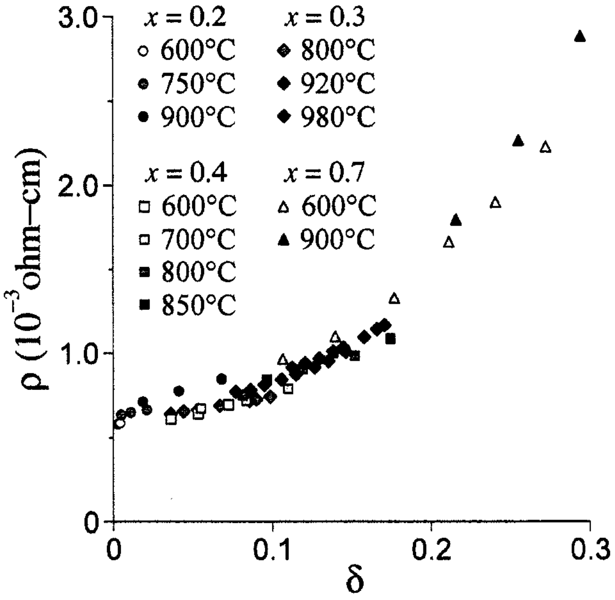

Figure 6-6: Electrical resistivity of LSC as a function of oxygen vacancy concentration at different temperatures (color/grayscale) and Sr content (x) (symbols). Data for x = 0.3 and x = 0.7 taken from references [92] and [50], respectively.

One might consider two possible explanations for the behavior shown in *Figure 6-5* at T ≥ 800 C. The first is competing effects: as oxidation state increases, magnetic moment increases due to increased occupation of the Co d-levels; but at the same time the Weiss field (and thus also θ) decreases due to increased bond length (chemical expansion); the net result being that the numerator and denominator in equation (2) scale equally with oxidation state. Besides being an amazing coincidence, our previous measurements of chemical expansion in LSC family of materials show that bond length scales with vacancy concentration, not oxidation state [78]. Thus this theory fails to explain the universality of χ vs x, since materials of differing x would be expected to have different Weiss fields.

This leaves us with a second explanation for the data in *Figure 6-5* at T ≥ 800 C: the electron states associated with changes in oxidation state are itinerant,[50, 72] and thus contribute only a small Pauli susceptibility. Since these states do not contribute to χ, no changes in χ are seen in with electron occupation. As the temperature is lowered, some dependence of χ on electron occupancy appears, possibly suggesting the onset of localization effects. This dependence becomes stronger with decreasing x, consistent with the fact that LSC undergoes a metal to semiconductor transition with decreasing x in this range of x and T[50, 72].

As summarized in the Introduction, there appears to be general agreement that the metallic state of LSC involves a partially occupied delocalized σ* band, formed by hybridization of oxygen 2p and 3d e_g orbitals.[21, 30, 44, 53, 55, 93, 94] However, it remains a matter of debate whether the spin state of Co is intermediate spin, or transitional to high spin.[38, 54, 55, 95-98] Density functional calculations [53] and thermal expansion studies [57] indicate that Co^{3+} is most likely to be in an intermediate spin configuration at the highest temperatures.

Assuming LSC is intermediate spin, the resulting electronic structure near the Fermi level is depicted in Figure 6-7a. At an electron occupation number of zero (i.e. $\delta = x/2$), the Fermi level would be expected sit in the middle of the σ* band, resulting in metallic properties. Decreasing δ or substitution of Sr^{2+} for La^{3+} would increase the Co oxidation state, resulting in a lowering of electron occupation in the σ* band. In this scenario, we would expect the magnetic susceptibility to be insensitive to moderate shifts in oxidation state, since the electrons are added or removed from the delocalized σ* band. Any small changes in Pauli susceptibility due to band curvature would be expected to be immeasurably small.

In contrast, as the occupation of the σ* band continued to decrease, the Fermi level might drop into the range of more localized t_{2g} (t^2_β) states. Alternatively, these localized states might rise to the Fermi level due to localized Jahn-Teller distortions. [53, 57] In both cases, the Fermi level would then sit such that valence electrons comprise a mixture of localized t_{2g} (t^2_{β}) states with the delocalized σ^* states, as depicted in Figure 6-7b. In this regime, any change in oxidation state would be expected to involve both localized and delocalized states, and thus measurably influence the paramagnetic susceptibility.

The data in *Figure 6-5* show that above 800°C the magnetization is almost completely independent of oxidation state over nearly its entire accessible range - up to $^1/_3$ electron per Co atom relative to Co^{3+}. This observation suggests that active valence electrons are part of a purely intermediate spin configuration at the highest temperatures, since even the largest changes in band occupancy are too small to lower the Fermi level into the range of more localized states. In contrast, at 710 °C, the observed dependence of magnetization on electron occupancy appears across the entire range of oxidation states, and an explicit dependence on Sr content also emerges. This effect appears to be most consistent with an upward shift in energy of t_b^2 states relative to s* states, resulting in partial localization of the valence electrons at all oxidation states.

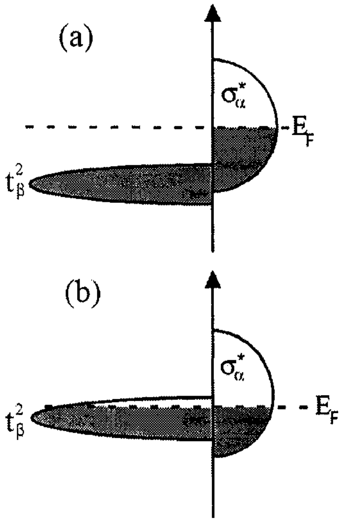

Figure 6-7: Schematic of the electronic structure of LSC near the Fermi level at high temperatures. a) Purely intermediate spin (IS) configuration involving a partially filled delocalized σ band. b) Partially localized configuration in which the Fermi level overlaps localized t_β^2 states. This figure based on a more complete qualitative diagram in reference.*[55]

Figure 6-8 shows a plot of logarithm of electrical conductivity vs 1/T at different electron occupancy (n_e) for LSC 8210 and LSC 6410. This plot shows that conductivity becomes metallic at temperatures higher than 700^{0}C in both the samples studied. Conductivity decreases with increase in electron occupancy, which can be attributed to electron scattering effects of high oxygen vacancy concentration in the lattice. At temperatures higher than 700^{0}C, both samples show non-activated behavior consistent with magnetization dependence on electron occupancy. The temperature dependence of electrical conductivity may provide further evidence for the arguments presented above.

(a)

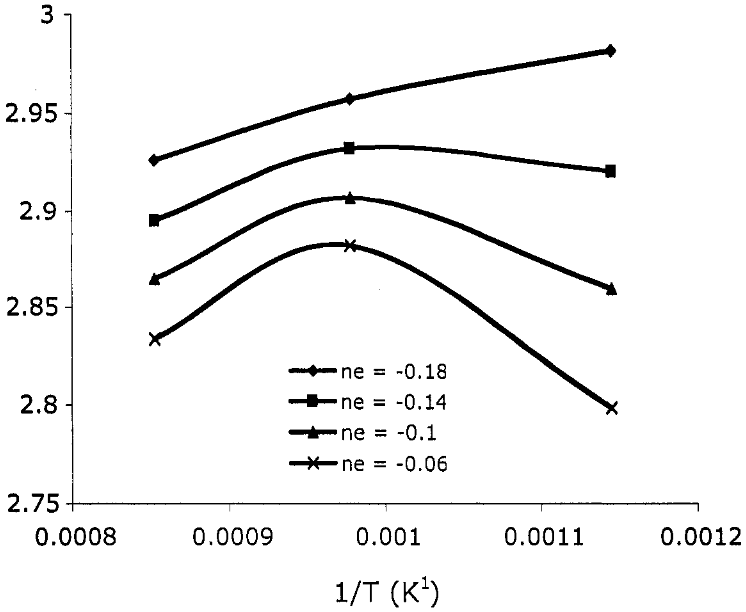

(b)

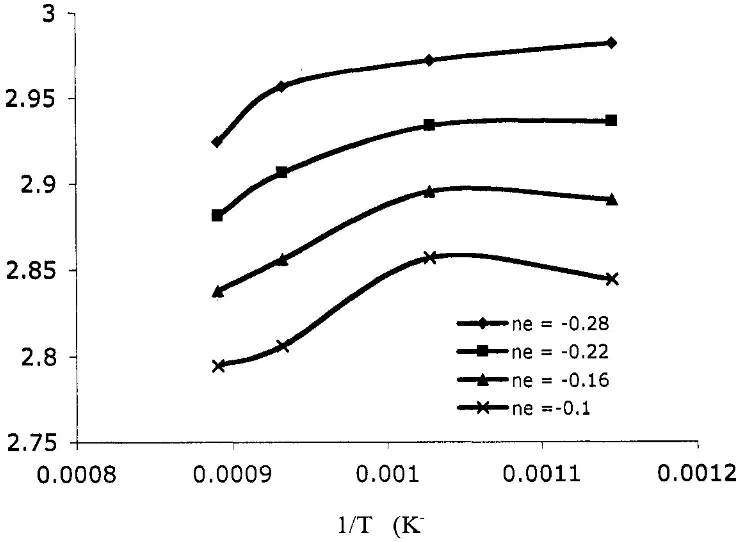

Figure 6-8: Activation energy plot for conductivity based on Figure for (a) LSC 8210 and (b) LSC 6410 at different electron occupancy values in the material.

In order to differentiate increases in resistance with temperature from those associated with defect scattering, it is helpful to consider Matthiessen's rule for dilute alloys, which treats the superposition of these effects:[99]

$$\rho = \rho_T + \rho_D \qquad (3)$$

where $\rho_T(T)$ is resistance associated with phonon scattering in a normal lattice, and ρ_D (assumed independent of temperature), represents additional scattering associated with point defects. Assuming LSC remains metallic with fixed density of states at the Fermi level, $\rho_T(T)$ would be expected to be close to linear (with a coefficient only weakly dependent of Sr content), while $\rho_D(\delta)$ would be expected to be a universal function. Under these assumptions equation (3) can be rearranged as:

$$\rho_D(\delta) = \rho - \alpha T \qquad (4)$$

where $\alpha(x)$ is the thermal resistance coefficient.

Figure 6-9 shows a plot of $\rho_D(\delta)$, obtained using equation 4 by assuming various values of $\alpha(x)$ that suppress $\rho_D(\delta)$ at $\delta = 0$. The values of $\alpha(x)$ so obtained are very similar for all materials, as shown in

Figure 6-9 (inset). The resulting plot of $\rho_D(\delta)$ exhibits a nearly universal trend of resistance vs. defect concentration, supporting the view that LSC is metallic, with a broad conduction band that sees very little change in density of states at the Fermi level. The universality of this trend is weakest for temperatures below ~800°C (light colored symbols), consistent with the view that localized states may start to become important at all oxidation states below a certain temperature, accompanied by a breakdown in Matthiessen's rule. Both the magnetic measurement and electrical resistivity as a function of oxygen vacancy concentration point to metallic behavior of LSC at temperature above 800^0C.

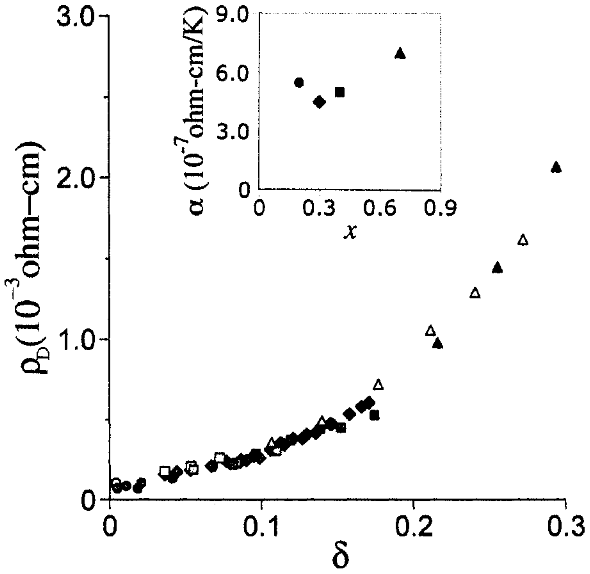

Figure 6-9: Contribution of defect scattering to electrical resistivity of LSC, calculated from the data in Figure 6-6 according to equation (4) assuming various values of the thermal resistance coefficient (inset). Symbols and color/grayscale as in Figure 6-6.

The above explanation of LSC's high-temperature magnetic properties in terms of an approach to a purely IS configuration is only partially satisfying, since it does not fully explain the persistence of Curie-Weiss susceptibility at high temperature. To get an estimate of the number of unpaired spins in the system, equation (2) can be rearranged to give a relation between the number of Bohr magnetons (*p*) per cobalt ion and magnetic susceptibility:

$$p^2 = \frac{\chi(T-\theta)3k}{\mu_0 N \mu_B^2} \quad (5)$$

Equation (5) yields ~3.5 Bohr magnetons, consistent with measurements of the saturation moment at low temperatures. [53, 55, 57] Figure 6-10 shows estimated number of Bohr magnetons extracted at two different electron occupancy. The value of Bohr magnetons show negligible change with temperature and electron occupancy. This large experimental value has been rationalized in terms of orbital contribution to the spin only

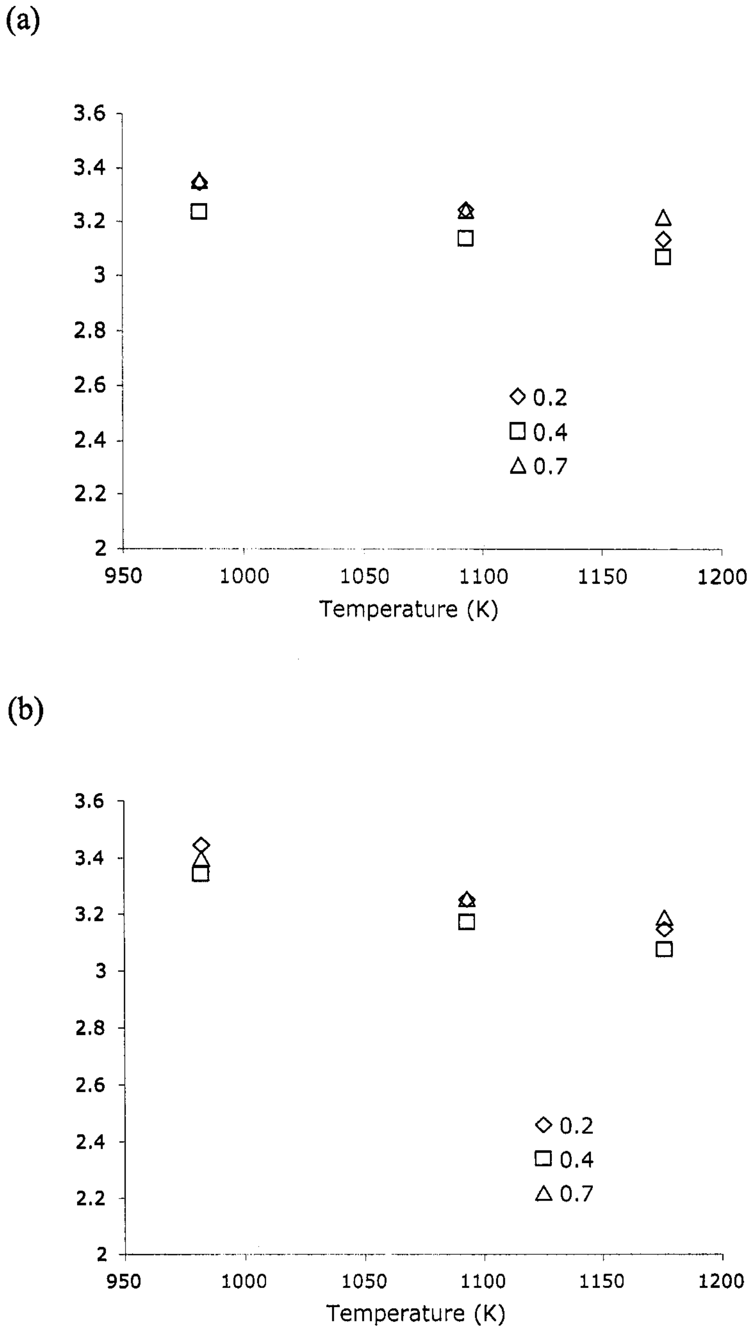

Figure 6-10: Estimated number of Bohr magnetons for LSC of three different strontium compositions at (a) zero electron occupancy (b) electron occupancy of -0.2

value of the effective magnetic moment (2.83 μ_B) considering the electrons in the IS Co^{3+} configuration.[53] However, if this were the correct explanation, one might expect a much smaller paramagnetic moment at high temperatures, since (according to our measurements here) the valence electrons do not contribute to the localized electron population.

Preliminary measurements of magnetic susceptibility at intermediate temperatures were carried out in LSC-37. Figure 6-11 shows the measured values as a function of oxygen vacancy concentration, along with previously measured values of magnetic susceptibility in the high temperature range. Interestingly, the oxidation state dependence of magnetic susceptibility becomes stronger as temperature is lowered. This suggests that the electron states associated with oxygen exchange is closely related to the localized electron states, rather than delocalized 3d-electron states.

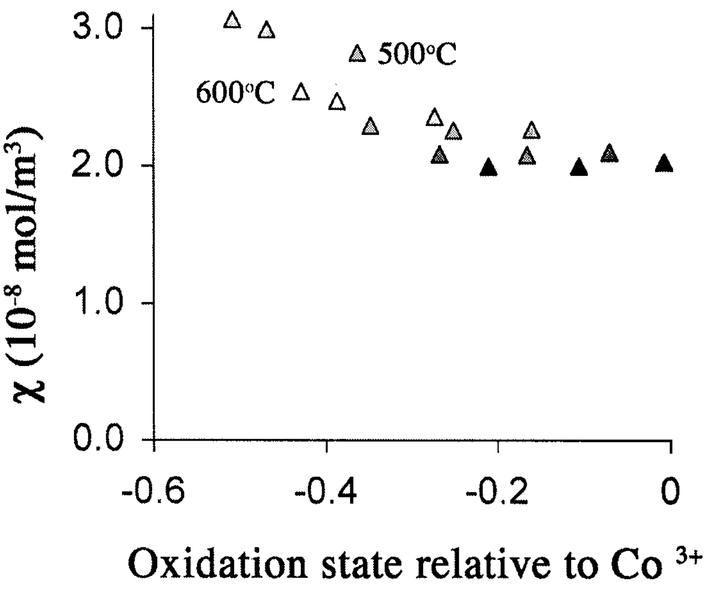

Figure 6-11: Magnetic susceptibility of LSC-37 in the intermediate temperature range

6.4 Summary

In general the observation of Curie-Weiss susceptibility (rather than Pauli susceptibility) in metallic oxides above their magnetic ordering temperatures is not very well understood.[10] One possible resolution to this paradox is that the material is not homogeneous at a local atomic level, evidence for this possibility includes recent ^{139}La NMR measurement showing the co-existence of ferromagnetic and non-ferromagnetic phases in LSC for various Sr dopant levels at low temperatures.[41] Evidence of phase separation has also been recently observed in a similar perovskite, $Nd_{1-x}Sr_xCoO_3$ using NMR.[100] The σ* electrons participating in changes in oxygen nonstoichiometry may themselves represent only a fraction of the e_g electrons in the system, many of which may be tied up in localized domains.

Thus, even though the valence electrons in LSC are itinerant at high temperatures, a significant fraction of the material may possess a more localized high spin configuration involving fixed Co oxidation state (which does not participate in oxygen exchange). Perhaps, as the temperature is lowered these localized states become increasingly important for the oxygen nonstoichiometry, leading to oxygen vacancy dependence of magnetic susceptibility. Measurements of magnetic susceptibility at high temperature suggest that above ~800^{0}C, the material possesses itinerant valence electrons, which is consistent with the electrical conductivity, Seebeck coefficient and oxygen nonstoichiometry properties of LSC.

Chapter 7. Modification of rigid electron band model to predict oxygen vacancies in LSC

7.1 *Introduction*

Lankhorst and coworkers have shown that oxygen non-stoichiometry can be predicted over a wide range of conditions using an itinerant electron model for metallic oxides like $La_{1-x}Sr_xCoO_{3-\delta}$ and $La_{1-x}Sr_xCo_{1-y}Fe_yO_{3-\delta}$ (LSCF)[101]. The primary assumption of this model is that electron entropy is roughly constant, while system energy depends on electron occupation within a wide metallic band. Although the validity of the electron gas rigid band has been questioned [102], the evidence that the chemical potential of electron decrease almost linearly with electron occupancy instead of oxygen nonstoichiometry strongly supported the applicability of this model for the oxygen-deficient perovskites $La_{1-x}Sr_xCoO_{3-\delta}$.

However, uncertainties remain regarding the nature of parameters used to obtain the optimum fit to experimental values of oxygen nonstoichiometry. For example, the variation in energetic and entropic parameters used in the fit cancel each other resulting in a more uniform variation of chemical potential with electron occupancy. However, the measured values of entropy using coulometric titration showed significant nonlinearities[46]. The rigid band model fits reasonably well at high temperature range (>800 ^{0}C) where LSC is metallic[46], but deviates from experimental values at temperatures less than 800 ^{0}C. Magnetic measurements discussed in chapter 6 showed inhomogeneous electronic structure, indicating the presence of localized spin domains even at high temperatures. In this chapter, we attempt to model oxygen nonstoichiometry based on additional parameters, which reflects localized electron and hole states, along with the parameters from original model.

7.2 Rigid band model: Review

Lankhorst's *rigid electron model* is based on the assumption that the electrons created during oxygen vacancy formation are donated to electron states of a partially filled metallic electron band[101, 103, 104]. Oxygen incorporation reaction can be written with Kröger-Vink notation[105] as:

$$O_2^{gas} + 2V_O^{\bullet\bullet} + 4e' \rightleftharpoons 2O_O^{\times} \qquad (1)$$

where $V_O^{\bullet\bullet}$ represents oxygen vacancies, e' conduction electrons, and $O_O^{\times}$ regular lattice oxygen ions. Under equilibrium, the chemical potential of oxygen in the sample must equal the chemical potential of gas phase, equated as:

$$\mu_{O_2}^{oxide} + 2\left(\mu_{V\ddot{O}} - \mu_{O\overset{\times}{O}}\right) + 4\mu_{e'} = 0 \qquad (2)$$

where μ_i denotes the chemical potential of species *I*, the chemical potential of oxygen vacancy and regular oxygen ions are obtained by further assuming oxygen vacancies and regular oxygen ions are distributed randomly among equivalent oxygen sites and do not interact each other[103, 104]:

$$\begin{aligned} \mu_{V_O^{\bullet\bullet}} &= \mu^0_{V_O^{\bullet\bullet}} + RT\ln\delta \\ \mu_{O_O^{x}} &= \mu^0_{O_O^{x}} + RT\ln(3-\delta) \end{aligned} \qquad (3a,b)$$

where superscript "0" denotes the standard state, δ oxygen nonstoichiometry equivalent to the mole fraction of oxygen vacancies $[V_O^{\bullet\bullet}]$. Substituting eqn (3a,b) into eqn (2), the chemical potential of oxide and oxygen gas under equilibrium is given by:

$$\mu^0_{O_2}(T) + RT\ln P_{O_2} = E_{ox} - TS_{ox} - 2RT\ln\left(\frac{x_v}{1-x_v}\right) - 4E_F \qquad (4)$$

where $\mu^0_{O_2}(T)$ is the standard oxygen chemical potential (a known function of temperature), $E_{ox} = 2\varepsilon^0_{O_O^X} - 2\varepsilon^0_{V_O^{\bullet\bullet}} - 4\varepsilon^0_{e'}$ and $S_{ox} = 2s^0_{O_O^X} - 2s^0_{V_O^{\bullet\bullet}}$ are the respective energy and entropy terms associated with placing an oxygen molecule from vacuum into the oxide by filling up two vacant oxygen lattice sites while placing four electrons at the Fermi level (E_F). The primary assumption of rigid band model is that electron entropy remains constant, while electron energy depends linearly on electron occupation within a metallic band. Hence, when oxygen vacancy is formed by pulling an oxygen atom out of the bulk, the average oxidation state of cobalt must decrease, resulting in an increase in electron energy. $E_F = (6x_v - x)/g_0$ is the Fermi energy measured relative to its vale at full oxygen nonstoichiometry, where g_0 is the density of states at the Fermi level, assumed to be constant.

Although the model predicts linearity of chemical potential with oxygen vacancy concentration, the enthalpy and entropy parts of free energy show significant deviation from linearity. In order to get an estimate the enthalpy of oxidation in LSC and how it varies with oxygen vacancy concentration, room temperature calorimetric studies were carried out on samples quenched at different temperatures and oxygen partial pressures. Table 7-1 gives the value of enthalpy of oxidation for different oxygen nonstoichiometry (theoretical and experimental) values based on the quenching conditions. Experimental determination of oxygen nonstoichiometry values was carried out by TGA measurements, reasonable agreement was observed between theoretical and experimental values of oxygen nonstoichiometry in samples. Figure 7.1 shows a plot of enthalpy of oxidation as a function of oxygen vacancy concentration. This plot shows that enthalpy of oxidation is independent of oxygen vacancy concentration, within experimental error. This behavior contradicts the linear dependence predicted by rigid band model. Interestingly, the magnitude of enthalpy of oxidation (~106 kJ/mol of oxygen molecule) is ~2 times smaller than the predicted values from the model.

One possible explanation for this difference in magnitude is temperature of measurements: calorimetric studies yield room temperature values of enthalpy while the rigid band model predicts values at high temperatures. This data suggest that energy associated with oxygen vacancy formation in LSC is nearly constant. The rigid electron band is useful for predicting the oxygen nonstoichiometry values in LSC as a function of temperature and oxygen partial pressure in reasonable agreement with experimental values. However, the variation of fitting parameters with strontium composition and trends observed are yet to be clearly understood.

Table 7-1. *Thermochemical data for* $La_{0.6}Sr_{0.4}CoO_{3-\delta}$ *(all values in kJ per mole of sample)* (Uncertainties are two standard deviations of the mean, numbers in parentheses are the number of experiments performed)

δ (theoretical)	**δ (measured)**	**ΔH_{ox} (Eq. 3)**
0.212	0.198± 0.06	-26.60 ± 6.83
0.171	-	-29.97 ± 6.89
0.159	0.154± 0.05	-28.60 ± 6.91
0.115	-	-28.25 ± 6.93
0.091	-	-32.37 ± 6.82
0.086	0.081± 0.008	-30.33 ± 6.96
0.086	-	-30.92± 6.96
0.059		-35.58 ± 6.83
0.054	0.041± 0.008	-37.32 ± 6.84
0.026	-	-35.98 ± 6.87

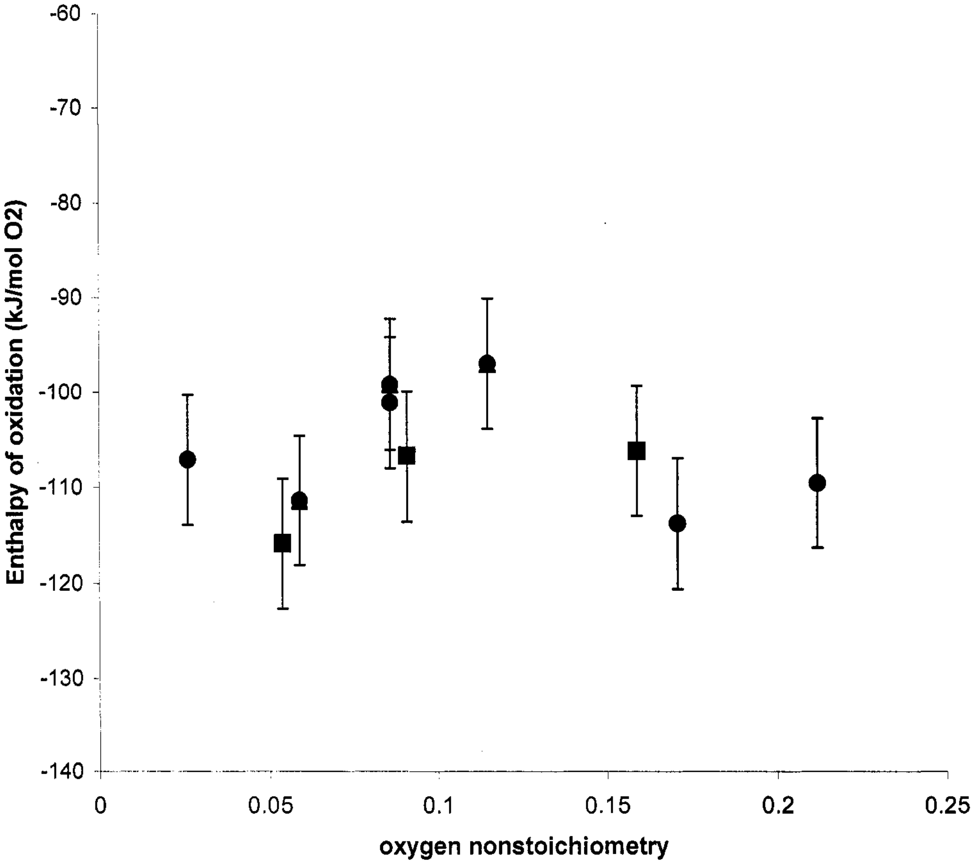

Figure 7-1:Enthalpy of oxidation as a function of oxygen nonstoichiometry, samples are quenched at different temperatures: 897C(●), 792C(■) and 702C(▲)

7.3 Modifications to rigid band model

In chapter 6, we discussed the high temperature magnetic behavior of LSC in terms of inhomogeneos electronic structure. In this modification, we consider the localized electron states along with the rigid band approximation from the original model. In the rigid band model, the Fermi level varies as a function of oxygen vacancy concentration and is related to the density of states at the Fermi level(g_0) by the relation:

$$E_F = \frac{(6x_v - x)}{g_0} \qquad (5)$$

In our modification to the rigid band model, we assume wide band assumption is valid for metallic region , and consider the effect of localized electron and hole states on Fermi level. In this case, electroneutrality is altered due to the presence of additional charge carriers and equation (5) is modified to reflect this as

$$E_F = \frac{(6x_v - x + n_h - n_e)}{g_0} \qquad (5)$$

where n_e and n_h represent the concentration of electrons and holes that are localized. We consider these localized charge carriers as semiconductors: holes (in valance band) and electrons(in conduction band). This modification is shown schematically in *Figure 7-2.* Fermi level of zero indicate perfect stoichiometry in the sample (or Co^{3+}) and Egap represent the band gap between the valance band and the conduction band. We also introduce a parameter, ΔE , representing the difference in energy between $E_F = 0$ and $E_{gap}/2$. With these additional parameters, the concentration of electrons and holes can be written (as a function of E_F) as :

$$n_e = N_{CB} \exp \frac{-\left(\frac{E_{gap}}{2} + \Delta E - E_F \right)}{RT} \qquad (6)$$

$$n_h = N_{VB} \exp \frac{-\left(E_F + \frac{E_{gap}}{2} - \Delta E \right)}{RT} \qquad (7)$$

where N_{CB} and N_{VB} is the number of available states in the conduction band and valance band respectively. Combining equations(4), (5), (6) and (7) one can estimate oxygen nonstoichiometry as a function of Temperature and oxygen partial pressure using thermodynamic parameters E_{ox}, S_{ox} and g_0. For very large values of band gap, the concentration of localized electrons and holes do not alter the occupancy of the rigid band and hence the modifications simplify to original model. We applied this *modified rigid electron band model* to fit the experimental nonstoichiometry data of $La_{1-x}Sr_xCoO_{3-\delta}$ (x=0.2, 0.4, and 0.7) from literature and for a wide range of temperature and oxygen partial pressure.

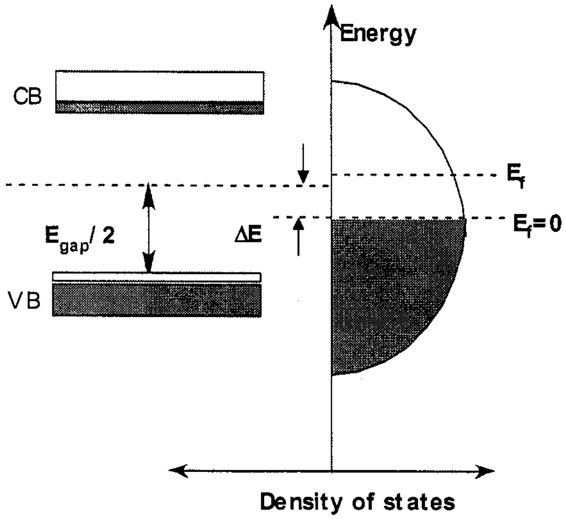

Figure 7-2:Illustration showing electron and holes states along with wide band approximation of rigid band model

The experimental values at each temperature is fitted with the modified model to estimate thermodynamic parameters as a function of temperature. This is useful in determining the trends, if any, of various fitting parameters used as a function of temperature. Figure 7.3 through Figure 7.5 show the fit obtained for experimental values of oxygen nonstoichiometry for LSC 82, LSC 64 and LSC 37 respectively. The modified model fits experimental values of oxygen nonstoichiometry better than the reported fit[46] from original model. Table 7-2 shows the value of thermodynamic parameters used to obtain this fit for these three compositions of LSC. The order of magnitude and dependence of parameters, E_{ox} and S_{ox} with Sr content in LSC are consistent with the original rigid band model. The entropic parameter Sox is treated as a function of strontium composition only and was held constant during the fitting procedure. The temperature effects on E_{ox} variation is insignificant and in general the se values are close to values obtained from original model.

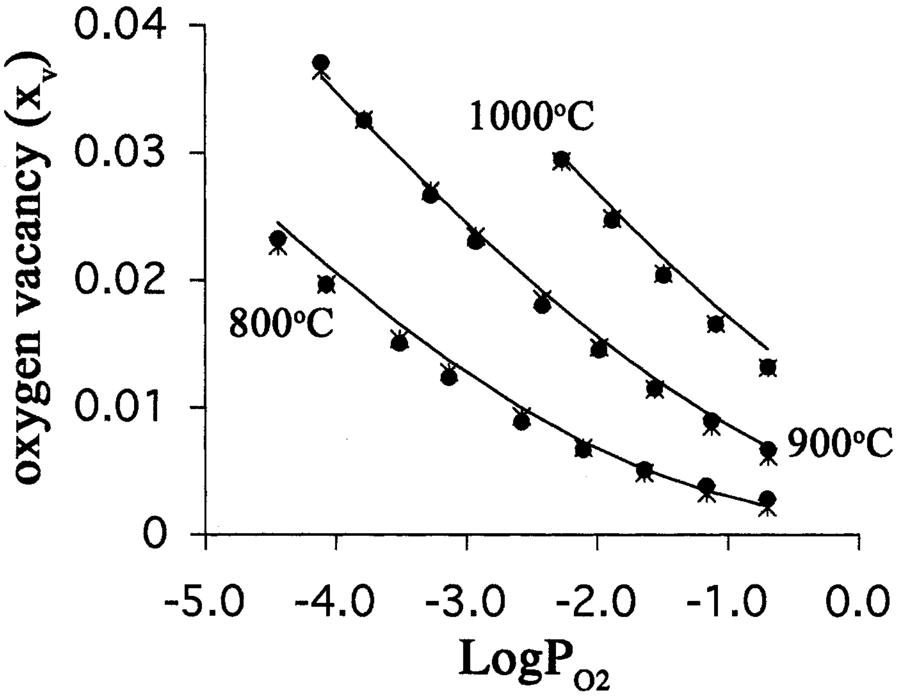

Figure 7-3: Experimental values of oxygen nonstoichiometry(symbols •) and predicted values (x) as a function of oxygen partial pressure at different temperatures for LSC 82. Drawn lines are fitting based on original rigid band model.

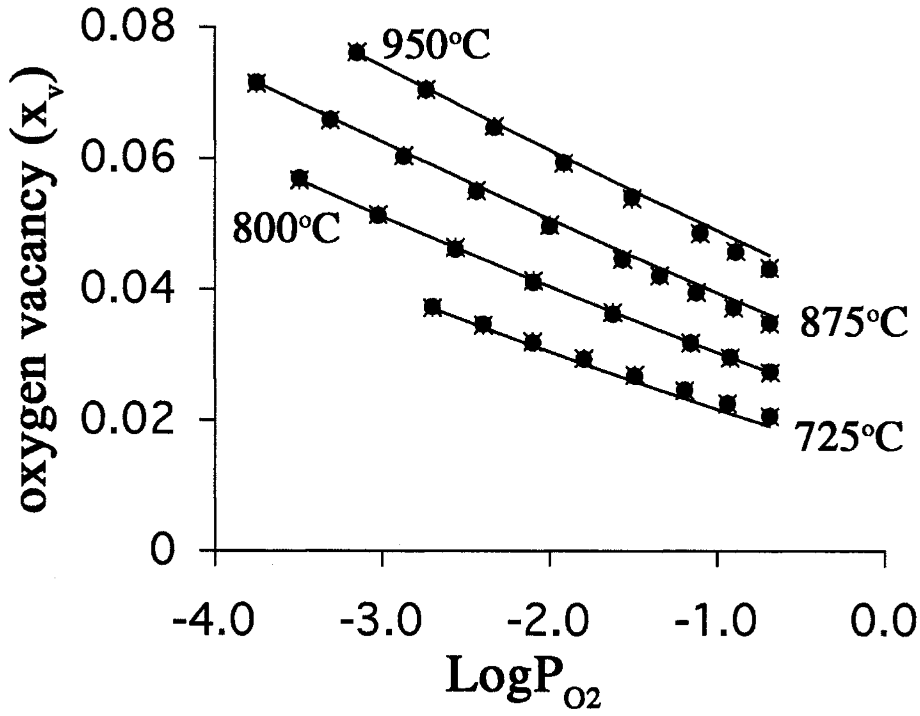

*Figure 7-4:Experimental values of oxygen nonstoichiometry(symbols •) and predicted values (*x*) as a function of oxygen partial pressure at different temperatures for LSC 64. Drawn lines are fitting based on original rigid band model.*

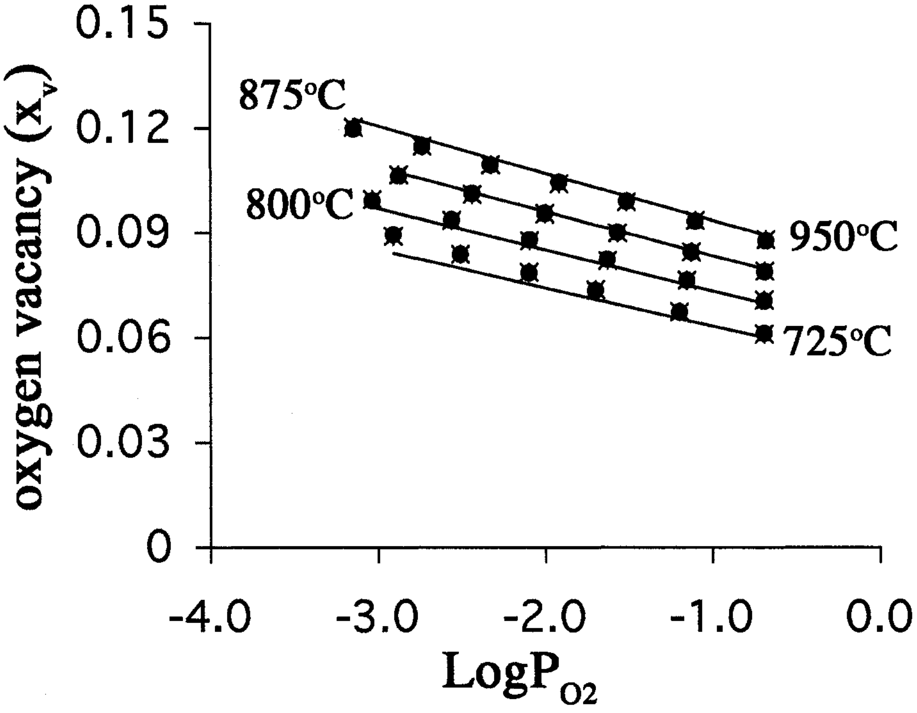

Figure 7-5: Experimental values of oxygen nonstoichiometry(symbols •) and predicted values (x) as a function of oxygen partial pressure at different temperatures for LSC 37. Drawn lines are fitting based on original rigid band model.

Table 7-2. Parameters obtained from modified itinerant electron model for different strontium compositions

	x=0.2 Temperature(°C)		
	1000	**900**	**800**
Eox (kJ/mol)	334.4	333.9	340.2
Sox (J/mol.K)	69.5	69.5	69.5
g0 (mol/kJ)	188.0	175.9	145.2
ΔE (kJ/mol)	7.4	3.1	9.9
E_{gap} (kJ/mol)	509.3	426.8	1277.8

	x=0.4 Temperature(°C)			
	725	**800**	**875**	**950**
Eox (kJ/mol)	307.0	301.3	302.1	302.3
Sox (J/mol.K)	69.6	69.6	69.6	69.6
g0 (mol/kJ)	140.7	159.8	166.6	173.7
ΔE (kJ/mol)	0.3	0.5	0.4	0.4
E_{gap} (kJ/mol)	1158	1042	980	933

	x=0.7 Temperature(°C)			
	950	**875**	**800**	**725**
E_{ox}(kJ/mol)	298.5	295.7	289.9	279.9
S_{ox}(kJ/mol)	70.5	70.5	70.5	70.5
g0 (mol/kJ)	187.5	165.7	158.44	152.6
ΔE(kJ/mol)	-1.6	-1.9	12.5	21.2
E_{gap}(kJ/mol)	308	396	415	235

However, there are no systematic variations of additional parameters introduced in the modification (E_{gap} and ΔE) with temperature. Also, the estimated value of band gap is very large compared to values in typical semiconductors (~96 kJ/mol) and the difference in Fermi levels (ΔE) is insignificantly small compared to the band gap values predicted by the model. The values of these parameters, obtained from the fit, suggest that the concentration of n_h and n_e are too small to have a significant effect on the electroneutratlity of equation (5). This suggests that treating electron and hole states using band gap and the energy difference between the Fermi level do not quite explain the better fit obtained using the modified model.

The parameter from the fit that do show systematic variation, in all three compositions, is the density of states at the Fermi level (g_0). The modified model predicts that g_0 increases with increase in temperature, while the original model assumed constant g_0 for all temperatures. One possible explanation for this trend is that the electron energy states constituting the rigid band splits into empty unoccupied states and filled states, at low temperatures as shown in Figure 7-6. This picture shows schematically a system with localized (occupied and unoccupied states with narrow band) and delocalized electrons at low temperature evolving towards a more uniform rigid band (dotted lines) at high temperatures. In this scenario, g_0 decreases with decrease in temperature due to the formation of localized electron state, as shown in Figure 7-6.

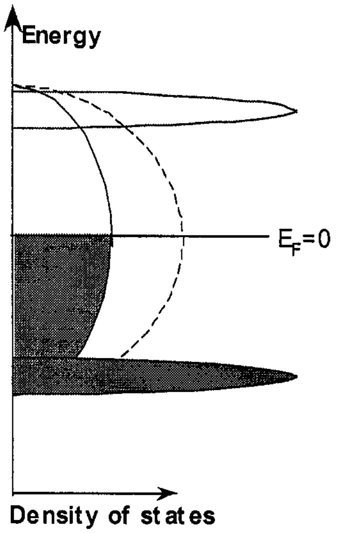

Figure 7-6: Schematic showing possible effects of electron localization with decrease in temperature.

High temperature magnetic property of LSC, discussed in chapter 6, showed that as temperature is reduced the magnetic susceptibility became increasingly dependent on cobalt oxidation state suggesting localization effect. As shown in Figure 6-11, at lower temperatures (<700 C) LSC 37 showed increasing dependence of magnetic susceptibility on electron occupancy. The predicted trend from the modified model for g_0 matches this experimental observation in magnetic properties of LSC. Although magnetic susceptibility of LSC shows stronger dependence on oxidation state with decreasing temperature, the energy of these localized states can be well below the Fermi level to influence the oxygen nonstoichiometry behavior. This modification of the rigid band model illustrates the effect of density of states shift (due to electron localization) on predicting oxygen nonstoichiometry as a function of temperature and oxygen partial pressure.

7.4 Summary

In this chapter, we have extended the idea of inhomogeneous electronic structure in LSC to predict oxygen nonstoichiometry as a function of temperature and oxygen partial pressure. We introduced additional parameters, ΔE and E_{gap} to reflect localized electrons and holes in the system (in concurrence with metallic region obeying rigid band formalism for LSC). It was determined that the energy gap between the valance band and conduction band representing these localized states are large enough to make any significant contribution to electro-neutrality. On the other hand, we found that the density of states at the Fermi level (g_0) is a function of temperature: g_0 increases with increasing in temperature. A possible explanation for this behavior is that the electron energy states constituting the rigid band split into localized occupied and unoccupied states. This modification to the rigid band model predicts oxygen concentration values close to experimentally measured values over wide range of temperature and oxygen partial pressure.

Chapter 8. Conclusions and Future directions

In this work, we have presented a method to measure magnetic susceptibility of transition metal oxide perovskites at high temperatures as a function of oxygen partial pressure. This involved the design of a custom built Faraday magnetometer to measure magnetic susceptibility as a function of temperature and oxygen partial pressure. This method is effective to measure magnetic susceptibility at temperatures as high as 1000 C and oxygen partial pressure as low as 100ppm. These measurements serve us a useful probe to understand electronic structure in transition metal oxides with perovskite structure.

We have studied two systems of differing electronic structure: LSC and LSF at high temperatures. Electronic structure of these materials is closely associated with their defect structure. In order to address various issues including magnetic interaction, insulator to metal transition, an independent measurement of electronic structure as a function of oxygen vacancy defects is essential. By controlling the temperature and oxygen partial pressure in the Faraday magnetometer, we can attain wide variation in oxygen vacancy concentration. This enables us to separate the effect of temperature from the effect of oxidation state change of cations (Fe and Co) on electronic structure.

High temperature magnetic measurement of LSF shows strong temperature dependence and oxygen vacancy concentration dependence. However, the spin state of iron and its effect on magnetic interactions play an important role in determining how magnetization varies with changes in oxygen vacancy concentration. As the concentration of oxygen vacancies increase, the bond length increases resulting in weaker magnetic interaction and hence a lower magnetic susceptibility. These results are consistent with similar conclusions obtained for LSF based on neutron scattering measurements. The variation of magnetic interactions, based on magnetic susceptibility measurement, suggests that the interactions are strongly a function of oxygen vacancy concentration. Thus, high temperature magnetic behavior of LSF confirms that it has localized electronic structure.

On the other hand, high temperature magnetic measurements in LSC reveal a different aspect of electronic structure. High temperature magnetization suggests coexistence of localized and delocalized states. However, electrical conductivity measurements in the same temperature and oxygen partial pressure range suggest that LSC is metallic. In addition, Curie-Weiss susceptibility persists even in the metallic regime, with a total magnetic moment of 3.4 Bohr magnetons per Cobalt. Such a high value suggests localized 3d electrons are in an intermediate spin configuration for Co^{3+} and difficult to explain based on a homogeneous electronic structure. As temperature is increased, the electrons associated with electrical conductivity and oxygen vacancies become increasingly itinerant, and yet large population of localized paramagnetic center remains. We conclude that this behavior is indicative of inhomogeneous electronic structure, which leads to trapped electronic states that are not directly associated with oxygen vacancies or electron transport. This conclusion is generally consistent with studies of localized structure and dynamics in highly defective perovskites.

Oxygen vacancy and its dependence on temperature and partial pressure is a crucial parameter governing the properties of electrochemical ceramics. Although models based on band picture in predicting oxygen vacancies in the metallic regime, these models break down when we stray into the intermediate temperature range (500 - 700^{0}C). To accurately predict oxygen vacancy in LSC using physically relevant parameters over wide range of temperature and oxygen partial pressure, we used our understanding of electronic structure based on high temperature magnetization measurements. This approximation involved use of additional parameter related to change in localized electron concentration at low temperatures with increase in oxygen vacancy concentration in the system. Although the fitting based on new model is similar to the original model, the additional parameters introduced are based on incorporating the inhomogeniety of electronic structure observed in high temperature magnetization studies.

This work shows that high temperature magnetization measurement is a valuable tool to understand electronic structure of materials as a function of defect concentration. When coupled with transport measurements, can provide useful information to correlate electronic structure with observed properties such as electronic conductivity and oxygen transport. This method can be extended for measurements in low temperature ranges where LSC is transitional between semiconductor and metal (400 – 600 C) and higher temperatures (1000 – 1200 C) where LSC is most clearly metallic. This method can also be extended to study the effects of Fe substitution on the Co site and understand whether the electron states of Fe remain localized or form a hybrid band with Co-3d states.

References

1. Bouwmeester, H. J. M., Dense ceramic membranes for methane conversion. *Catalysis Today* **2003,** 82, (1-4), 141-150.

2. den Otter, M. W.; Boukamp, B. A.; Bouwmeester, H. J. M., Theory of oxygen isotope exchange. *Solid State Ionics* **2001,** 139, (1-2), 89-94.

3. Gellings, P. J.; Bouwmeester, H. J. M., Solid state aspects of oxidation catalysis. *Catalysis Today* **2000,** 58, (1), 1-53.

4. Steele, B. C. H., Ceramic ion conducting membranes. *Current Opinion in Solid State & Materials Science* **1996,** 1, (5), 684-691.

5. Steele, B. C. H., Materials for high-temperature fuel cells. *Philosophical Transactions of the Royal Society of London Series a-Mathematical Physical and Engineering Sciences* **1996,** 354, (1712), 1695-1710.

6. Steele, B. C. H.; Newnham, R. E.; Evans, A. G., Ceramics, composites and intergrowths. *Current Opinion in Solid State & Materials Science* **1997,** 2, (5), 563-565.

7. Steele, B. C. H., Oxygen-Transport and Exchange in Oxide Ceramics. *Journal of Power Sources* **1994,** 49, (1-3), 1-14.

8. Dell, R. M.; Steele, B. C. H., Materials for high-temperature fuel cells - Discussion. *Philosophical Transactions of the Royal Society of London Series a-Mathematical Physical and Engineering Sciences* **1996,** 354, (1712), 1710-1710.

9. Dokiya, M.; Mizusaki, J.; Yamamoto, O.; Yokokawa, H., Solid oxide fuel cells dedicated to Prof. H. Tagawa - Preface. *Solid State Ionics* **2000,** 132, (3-4), 157-158.

10. Cox, P. A., *Transition metal oxides: An introduction to their electronic structure and properties*. Oxford University Press: Newyork, 1992; p pp 296.

11. Goodenough, J. B., Metallic Oxides. *Abstracts of Papers of the American Chemical Society* **1992,** 203, 614-Inor.

12. Torrance, J. B., An Overview of Transition-Metal Oxides - the Relation between Conductivity, Optical-Absorption and Ionicity. *Abstracts of Papers of the American Chemical Society* **1992,** 203, 652-Inor.

13. Torrance, J. B.; Lacorro, P.; Asavaroengchai, C.; Metzger, R. M., Simple and Perovskite Oxides of Transition-Metals - Why Some Are Metallic, While Most Are Insulating. *Journal of Solid State Chemistry* **1991,** 90, (1), 168-172.

14. Adler, S. B.; Lane, J. A.; Steele, B. C. H., Electrode kinetics of porous mixed-conducting oxygen electrodes. *Journal of the Electrochemical Society* **1996,** 143, (11), 3554-3564.

15. Bouwmeester, H. J. M.; Den Otter, M. W.; Boukamp, B. A., Oxygen transport in La0.6Sr0.4Co1-yFeyO3-delta. *Journal of Solid State Electrochemistry* **2004,** 8, (9), 599-605.

16. tenElshof, J. E.; Lankhorst, M. H. R.; Bouwmeester, H. J. M., Oxygen exchange and diffusion coefficients of strontium-doped lanthanum ferrites by electrical conductivity relaxation. *Journal of the Electrochemical Society* **1997,** 144, (3), 1060-1067.

17. Yoo, J.; Verma, A.; Wang, S. Y.; Jacobson, A. J., Oxygen transport kinetics in SrFeO3-delta, La0.5Sr0.5FeO3-delta, and La0.2Sr0.8Cr0.2Fe0.8O3-delta measured by electrical conductivity relaxation. *Journal of the Electrochemical Society* **2005,** 152, (3), A497-A505.

18. Sahibzada, M.; Steele, B. C. H.; Barth, D.; Rudkin, R. A.; Metcalfe, I. S., Operation of solid oxide fuel cells at reduced temperatures. *Fuel* **1999,** 78, (6), 639-643.

19. Sahibzada, M.; Steele, B. C. H.; Hellgardt, K.; Barth, D.; Effendi, A.; Mantzavinos, D.; Metcalfe, I. S., Intermediate temperature solid oxide fuel cells operated with methanol fuels. *Chemical Engineering Science* **2000,** 55, (16), 3077-3083.

20. Steele, B. C. H., Materials for IT-SOFC stacks 35 years R&D: the inevitability of gradualness? *Solid State Ionics* **2000,** 134, (1-2), 3-20.

21. Goodenough, J. B., Localized to itinerant electronic transition in perovskite oxides - Preface. *Localized to Itinerant Electronic Transition in Perovskite Oxides* **2001,** 98, Vii-X.

22. Mineshige, A.; Izutsu, J.; Nakamura, M.; Nigaki, K.; Kobune, M.; Fujii, S.; Inaba, M.; Ogumi, Z.; Yao, T., Electrical property, crystal structure and oxygen nonstoichiometry of La1-xSrxCo0.2Fe0.8O3-delta. *Electrochemistry* **2000,** 68, (6), 515-518.

23. Petrov, a. N.; Kononchuk, O. F.; Andreev, a. V.; Cherepanov, V. a.; Kofstad, P., Crystal-Structure, Electrical and Magnetic-Properties of La1-Xsrxcoo3-Y. *Solid State Ionics* **1995,** 80, (3-4), 189-199.

24. Russo, U.; Nodari, L.; Faticanti, M.; Kuncser, V.; Filoti, G., Local interactions and electronic phenomena in substituted LaFeO3 perovskites. *Solid State Ionics* **2005,** 176, (1-2), 97-102.

25. Tokura, Y.; Okimoto, Y.; Yamaguchi, S.; Taniguchi, H.; Kimura, T.; Takagi, H., Thermally induced insulator-metal transition in LaCoO3: A view based on the Mott transition. *Physical Review B* **1998,** 58, (4), R1699-R1702.

26. Steele, B. C. H.; Hori, K. M.; Uchino, S., Kinetic parameters influencing the performance of IT-SOFC composite electrodes. *Solid State Ionics* **2000,** 135, (1-4), 445-450.

27. Ohno, Y.; Nagata, S.; Sato, H., Effect of Electrode Materials on the Properties of High-Temperature Solid Electrolyte Fuel-Cells. *Solid State Ionics* **1981,** 3-4, (AUG), 439-442.

28. Adler, S. B.; Reimer, J. A., High-temperature O-17 NMR as a probe of electron localization and structure in transition metal oxides. *Solid State Ionics* **1996,** 91, (3-4), 175-181.

29. Goodenough, J. B., General considerations. *Localized to Itinerant Electronic Transition in Perovskite Oxides* **2001,** 98, 1-16.

30. Goodenough, J. B., Localized-itinerant electronic transitions in oxides and sulfides. *Journal of Alloys and Compounds* **1997,** 262, 1-9.

31. Matsuura, T.; Tabuchi, J.; Mizusaki, J.; Yamauchi, S.; Fueki, K., Electrical-Properties of La2-Xsrxcoo4.1. Structure, Electrical-Conductivity, and Seebeck Coefficient of Single-Crystals (X = 0.0, 0.5, 1.0 and 1.5). *Journal of Physics and Chemistry of Solids* **1988,** 49, (12), 1403-1408.

32. Mineshige, A.; Inaba, M.; Yao, T. S.; Ogumi, Z.; Kikuchi, K.; Kawase, M., Crystal structure and metal-insulator transition of La1-xSrxCoO3. *Journal of Solid State Chemistry* **1996,** 121, (2), 423-429.

33. Goodenough, J. B., Jahn-Teller phenomena in solids. *Annual Review of Materials Science* **1998,** 28, 1-27.

34. Adler, S.; Russek, S.; Reimer, J.; Fendorf, M.; Stacy, a.; Huang, Q. Z.; Santoro, a.; Lynn, J.; Baltisberger, J.; Werner, U., Local-Structure and Oxide-Ion Motion in Defective Perovskites. *Solid State Ionics* **1994,** 68, (3-4), 193-211.

35. Woodward, P. M., Octahedral tilting in perovskites.1. Geometrical considerations. *Acta Crystallographica Section B-Structural Science* **1997,** 53, 32-43.

36. Woodward, P. M., Octahedral tilting in perovskites.2. Structure stabilizing forces. *Acta Crystallographica Section B-Structural Science* **1997,** 53, 44-66.

37. Macchesn.Jb; Jetzt, J. J.; Potter, J. F.; Williams, H. J.; Sherwood, R. C., Electrical and Magnetic Properties of System Srfeo3-Bifeo3. *American Ceramic Society Bulletin* **1966,** 45, (4), 413-&.

38. Senarisrodriguez, M. A.; Goodenough, J. B., Lacoo3 Revisited. *Journal of Solid State Chemistry* **1995,** 116, (2), 224-231.

39. Takeda, T.; Yamaguch.Y; Watanabe, H., Magnetic Structure of Srfeo3. *Journal of the Physical Society of Japan* **1972,** 33, (4), 967-&.

40. Topfer, J.; Goodenough, J. B., Ferromagnetic perovskites in the system LaMn1-xGaxO3 stabilized by dynamic Jahn-Teller deformations. *European Journal of Solid State and Inorganic Chemistry* **1997,** 34, (5), 467-479.

41. Hoch, M. J. R.; Kuhns, P. L.; Moulton, W. G.; Reyes, A. P.; Lu, J.; Wu, J.; Leighton, C., Evolution of the ferromagnetic and nonferromagnetic phases with temperature in phase-separated La1-xSrxCoO3 by high-field La-139 NMR. *Physical Review B* **2004,** 70, (17), -.

42. Caciuffo, R.; Rinaldi, D.; Barucca, G.; Mira, J.; Rivas, J.; Senaris-Rodriguez, M. A.; Radaelli, P. G.; Fiorani, D.; Goodenough, J. B., Structural details and magnetic order of La1-xSrxCoO3 (x <= 0.3). *Physical Review B* **1999,** 59, (2), 1068-1078.

43. Chainani, a.; Mathew, M.; Sarma, D. D., Electron-Spectroscopy Study of the Semiconductor-Metal Transition in La1-Xsrxcoo3. *Physical Review B* **1992,** 46, (16), 9976-9983.

44. Zhou, H. D.; Goodenough, J. B., X-ray diffraction, magnetic, and transport study of lattice instabilities and metal-insulator transition in CaV1-xTixO3 (0 <= x <= 0.4). *Physical Review B* **2004,** 69, (24), -.

45. Choy, K.; Bai, W.; Clarojrochkul, S.; Steele, B. C. H., The development of intermediate-temperature solid oxide fuel cells for the next millennium. *Journal of Power Sources* **1998,** 71, (1-2), 361-369.

46. Lankhorst, M. H. R.; Bouwmeester, H. J. M.; Verweij, H., High-temperature coulometric titration of La1-xSrxCoO3-delta: Evidence for the effect of electronic band structure on nonstoichiometry behavior. *Journal of Solid State Chemistry* **1997,** 133, (2), 555-567.

47. Mizusaki, J.; Mima, Y.; Yamauchi, S.; Fueki, K.; Tagawa, H., Nonstoichiometry of the Perovskite-Type Oxides La1-Xsrxcoo3-Omega. *Journal of Solid State Chemistry* **1989,** 80, (1), 102-111.

48. van der Haar, L. M.; den Otter, M. W.; Morskate, M.; Bouwmeester, H. J. M.; Verweij, H., Chemical diffusion and oxygen surface transfer of La1-xSrxCoO3-delta studied with electrical conductivity relaxation. *Journal of the Electrochemical Society* **2002,** 149, (3), J41-J46.

49. Lankhorst, M. H. R.; Bouwmeester, H. J. M.; Verweij, H., Use of the rigid band formalism to interpret the relationship between O chemical potential and electron concentration in La1-xSrxCoO3-delta. *Physical Review Letters* **1996,** 77, (14), 2989-2992.

50. Mizusaki, J.; Tabuchi, J.; Matsuura, T.; Yamauchi, S.; Fueki, K., Electrical-Conductivity and Seebeck Coefficient of Nonstoichiometric La1-Xsrxcoo3-Delta. *Journal of the Electrochemical Society* **1989,** 136, (7), 2082-2088.

51. Misture, S., **To be published.**

52. Liu, J.; He, L. Y.; Chen, G. G.; Su, W. H., A study on selected properties of La1-xSrxCoO3 and its application in sealed CO2 lasers. *Journal of Materials Science* **1997,** 32, (1), 203-206.

53. Korotin, M. a.; Ezhov, S. Y.; Solovyev, I. V.; Anisimov, V. I.; Khomskii, D. I.; Sawatzky, G. A., Intermediate-spin state and properties of LaCoO3. *Physical Review B* **1996,** 54, (8), 5309-5316.

54. Naiman, C. S.; Gilmore, R.; Dibartol.B, Interpretation of Magnetic Properties of Lacoo3. *Journal of Applied Physics* **1965,** 36, (3P2), 1044-&.

55. Senarisrodriguez, M. A.; Goodenough, J. B., Magnetic and Transport-Properties of the System La1-Xsrxcoo3-Delta (0-Less-Than-X-Less-Than-or-Equal-to-0.50). *Journal of Solid State Chemistry* **1995,** 118, (2), 323-336.

56. Zhou, J. S.; Goodenough, J. B.; Asamitsu, A.; Tokura, Y., Pressure-induced polaronic to itinerant electronic transition in La1-xSrxMnO3 crystals. *Physical Review Letters* **1997,** 79, (17), 3234-3237.

57. Zobel, C.; Kriener, M.; Bruns, D.; Baier, J.; Gruninger, M.; Lorenz, T.; Reutler, P.; Revcolevschi, A., Evidence for a low-spin to intermediate-spin state transition in LaCoO3. *Physical Review B* **2002,** 66, (2), -.

58. Kroger, F. A., *The chemistry of imperfect crystals.* second edition ed.; 1964; Vol. 2.

59. Mizusaki, J.; Sasamoto, T.; Cannon, W. R.; Bowen, H. K., Electronic Conductivity, Seebeck Coefficient, and Defect Structure of La1-Xsrxfeo3(X=0.1,0.25). *Journal of the American Ceramic Society* **1983,** 66, (4), 247-252.

60. Mizusaki, J.; Sasamoto, T.; Cannon, W. R.; Bowen, H. K., Electronic Conductivity, Seebeck Coefficient, and Defect Structure of Lafeo3. *Journal of the American Ceramic Society* **1982,** 65, (8), 363-368.

61. Mizusaki, J.; Yoshihiro, M.; Yamauchi, S.; Fueki, K., Nonstoichiometry and Defect Structure of the Perovskite-Type Oxides La1-Xsrxfeo3-Delta. *Journal of Solid State Chemistry* **1985,** 58, (2), 257-266.

62. Yoo, J.; Park, C. Y.; Jacobson, A. J., Determination of the equilibrium oxygen non-stoichiometry and the electrical conductivity of La0.5Sr0.5FeO3-x. *Solid State Ionics* **2004,** 175, (1-4), 55-58.

63. Shimony, U.; Knudsen, J. M., Mossbauer Studies on Iron in Perovskites La1-Xsrxfe03 (0[-X=-1). *Physical Review* **1966,** 144, (1), 361-&.

64. Macchesn.Jb, Mossbauer effect in the system SrFeO2.5-3.0. *Journal of Chemical Physics* **1964,** 41, (8), 2429-2434.

65. Takeda, T.; Yamaguch.Y; Tomiyosh.S; Fukase, M.; Sugimoto, M.; Watanabe, H., Magnetic Structure of Ca2Fe2O5. *Journal of the Physical Society of Japan* **1968,** 24, (3), 446-&.

66. Hummel, R. E., *Electronic properties of Materials*. Third ed.; Springer: NewYork, 2004.

67. Kittel, C., *Introduction to solid state physics*. 1995.

68. Chichester, *Basic solid state chemistry*. second ed.; West, A.R. John Wiley and Sons, Ltd.

69. Topfer, J.; Goodenough, J. B., Charge transport and magnetic properties in perovskites of the system La-Mn-O. *Solid State Ionics* **1997,** 101, 1215-1220.

70. Zhou, J. S.; Goodenough, J. B.; Dabrowski, B.; Klamut, P. W.; Bukowski, Z., Enhanced susceptibility in LNiO3 perovskites (L = La, Pr, Nd, Nd0.5Sm0.5). *Physical Review Letters* **2000,** 84, (3), 526-529.

71. Mexner, W.; Heinemann, K., An Improved Method for Relaxation Measurements Using a Faraday Balance. *Review of Scientific Instruments* **1993,** 64, (11), 3336-3337.

72. Mineshige, A.; Kobune, M.; Fujii, S.; Ogumi, Z.; Inaba, M.; Yao, T.; Kikuchi, K., Metal-insulator transition and crystal structure of La1-xSrxCoO3 as functions of Sr-content, temperature, and oxygen partial pressure. *Journal of Solid State Chemistry* **1999,** 142, (2), 374-381.

73. Mogensen, M.; Skaarup, S., Kinetic and geometric aspects of solid oxide fuel cell electrodes. *Solid State Ionics* **1996,** 86-8, 1151-1160.

74. tenElshof, J. E.; Lankhorst, M. H. R.; Bouwmeester, H. J. M., Chemical diffusion and oxygen exchange of La0.6Sr0.4Co0.6Fe0.4O3-delta. *Solid State Ionics* **1997,** 99, (1-2), 15-22.

75. Palmer, L. D., Sources of Error in Thermogravimetry - Balance Inclination and Specimen Temperature. *Journal of Physics E-Scientific Instruments* **1980,** 13, (9), 919-923.

76. Gitzen, W. H., Alumina as a ceramic material, **1970.**

77. Chen, C. S.; Zhang, Z. P.; Jiang, G. S.; Fan, C. G.; Liu, W.; Bouwmeester, H. J. M., Oxygen permeation through La0.4Sr0.6Co0.2Fe0.8O3-delta membrane. *Chemistry of Materials* **2001,** 13, (9), 2797-2800.

78. Chen, X. Y.; Yu, J. S.; Adler, S. B., Thermal and chemical expansion of Sr-doped lanthanum cobalt oxide (La-1-xSrxCoO3-delta). *Chemistry of Materials* **2005,** 17, (17), 4537-4546.

79. Cheng, J. J.; Navrotsky, A.; Zhou, X. D.; Anderson, H. U., Thermochemistry of La1-xSrxFeO3-delta solid solutions (0.0 <= x <= 1.0, 0.0 <= delta <= 0.5). *Chemistry of Materials* **2005,** 17, (8), 2197-2207.

80. Cherepanov, V. a.; Barkhatova, L. Y.; Petrov, a. N.; Voronin, V. I., Oxygen Nonstoichiometry and Crystal and Defect Structure of Prmno3+Y and Ndmno3+Y. *Journal of Solid State Chemistry* **1995,** 118, (1), 53-61.

81. Lankhorst, M. H. R.; Bouwmeester, H. J. M., Determination of oxygen nonstoichiometry and diffusivity in mixed conducting oxides by oxygen coulometric titration.1. Chemical diffusion in La0.8Sr0.2CoO3-delta. *Journal of the Electrochemical Society* **1997,** 144, (4), 1261-1267.

82. Mizusaki, J.; Yamauchi, S.; Fueki, K.; Ishikawa, a., Nonstoichiometry of the Perovskite-Type Oxide La1-Xsrxcro3-Delta. *Solid State Ionics* **1984,** 12, (MAR), 119-124.

83. Sogaard, M.; Hendriksen, P. V.; Mogensen, M., Oxygen nonstoichiometry and transport properties of strontium substituted lanthanum ferrite. *Journal of Solid State Chemistry* **2007,** 180, (4), 1489-1503.

84. Chen, X. Thermo-mechanical/structural properties and oxygen permeation behavior of mixed ionic electronic conductors. University of Washington, Seattle, 2007.

85. Yu, J. Chemical Expansion studies in LSC. Case western reserve univeristy, 2002.

86. Alrawwas, a. D.; Johnson, C. E.; Thomas, M. F.; Dann, S. E.; Weller, M. T., Mossbauer Studies on the Series La1-Xsrxfeo3. *Hyperfine Interactions* **1994,** 93, (1-4), 1521-1529.

87. Battle, P. D.; Gibb, T. C.; Lightfoot, P., The Crystal and Magnetic-Structures of Sr2Lafe3O8. *Journal of Solid State Chemistry* **1990,** 84, (2), 237-244.

88. Yang, J. B.; Yelon, W. B.; James, W. J.; Zhou, X. D.; Xie, Y. X.; Anderson, H. U.; Chu, Z., Magnetic and Mossbauer studies on oxygen deficient perovskite, La0.6Sr0.4FeO3-delta. *Journal of Applied Physics* **2002,** 91, (10), 7718-7720.

89. Yoon, S. H.; Kim, C. S., Charge disproportionation transition under external magnetic field in La1/3Sr2/3FeO2.96. *Journal of Applied Physics* **2005,** 97, (10), -.

90. Zhou, X. D.; Cai, Q.; Yang, J.; Kim, M.; Yelon, W. B.; James, W. J.; Shin, Y. W.; Scarfino, B. J.; Anderson, H. U., Coupled electrical and magnetic properties in (La,Sr)FeO3-delta. *Journal of Applied Physics* **2005,** 97, (10), -.

91. Zhou, H. D.; Goodenough, J. B., Electronic behavior of three oxygen non-stoichiometric Fe4+/Fe3+ oxoperovskites. *Journal of Solid State Chemistry* **2005,** 178, (12), 3679-3685.

92. Petrov, A. N.; Kononchuk, O. F.; Andreev, A. V.; Cherapanov, V. A.; Kofstad, P., Crystal Structure, Electrical and Magnetic Properties of La1-xSrxCoO3-y. *Solid State Ionics* **1995,** 80, (3-4), 189-199.

93. Rao, C. N. R. S., M.; Narayana, C., *Spin state transition in LaCoO3 and related materials.* Springer: Berlin, 2004; Vol. 234, p pp 1-21.

94. Yan, J. Q.; Zhou, J. S.; Goodenough, J. B., Ferromagnetism in LaCoO3. *Physical Review B* **2004,** 70, (1), -.

95. Abbate, M.; Fuggle, J. C.; Fujimori, a.; Tjeng, L. H.; Chen, C. T.; Potze, R.; Sawatzky, G. a.; Eisaki, H.; Uchida, S., Electronic-Structure and Spin-State Transition of Lacoo3. *Physical Review B* **1993,** 47, (24), 16124-16130.

96. Asai, K.; Yoneda, A.; Yokokura, O.; Tranquada, J. M.; Shirane, G., Two spin-state transitions in LaCoO3. *Journal of the Physical Society of Japan* **1998,** 67, (1), 290-296.

97. Toulemonde, O.; N'Guyen, N.; Studer, F.; Traverse, A., Spin state transition in LaCoO3 with temperature or strontium doping as seen by XAS. *Journal of Solid State Chemistry* **2001,** 158, (2), 208-217.

98. Yamaguchi, S.; Okimoto, Y.; Taniguchi, H.; Tokura, Y., Spin-state transition and high-spin polarons in LaCoO3. *Physical Review B* **1996,** 53, (6), R2926-R2929.

99. Ziman, J. M., *Electrons and Phonons: The theory of Transport Phenomena in solids*. Oxford University Press: New York, 1960; p pp 568.

100. Ghoshray, A.; Bandyopadhyay, B.; Ghoshray, K.; Morchshakov, V.; Barner, K.; Troyanchuk, I. O.; Nakamura, H.; Kohara, T.; Liu, G. Y.; Rao, G. H., Phase separation in Nd1-xSrxCoO3 using Co-59 NMR. *Physical Review B* **2004,** 69, (6),

101. Lankhorst, M. H. R.; tenElshof, J. E., Thermodynamic quantities and defect structure of $La_{0.6}Sr_{0.4}Co_{1-y}Fe_yO_{3-\delta}$ (y=0-0.6) from high-temperature coulometric titration experiments. *Journal of Solid State Chemistry* **1997,** 130, (2), 302-310.

102. McKinnon, W. R. a. S., L.S, Ionic and electronic contributions to the Li chemical potential in LixRuzMo6Se8. *Physical Review B* **1987,** 35, (13), 7275-7279.

103. Lankhorst, M. H. R.; Bouwmeester, H. J. M.; Verweij, H., Thermodynamics and transport of ionic and electronic defects in crystalline oxides. *Journal of the American Ceramic Society* **1997,** 80, (9), 2175-2198.

104. Lankhorst, M. H. R.; Bouwmeester, H. J. M.; Verweij, H., High-temperature coulometric titration of $La_{1-x}Sr_xCoO_{3-\delta}$: Evidence for the effect of electronic band structure on nonstoichiometry behavior. *Journal of Solid State Chemistry* **1997,** 133, (2), 555-567.

105. Kroger, F. A., *Chap. 9*. 2nd ed.; 1964; Vol. 2.

CURRICULUM VITAE

Dinesh Baskar

Education

University of Washington, Seattle
PhD in Chemical Engineering, June 2008

University of Washington, Seattle
M.S in Chemical Engineering, June 2005

Central Electrochemical Research Institute, India
B.S in Chemical and Electrochemical Engineering, May 2002

Research Interests

Electrochemistry, Ceramics, Thin films, Fuel cells, Renewable energies and Batteries.

Honors and Awards

UW Graduate School Fund for Excellence and Innovation (GSFEI)– Travel funding from the UW Graduate School to attend SOFC-X conference in Nara, Japan. (Spring 2007)

Dokia Travel award – Travel funding from the Electrochemical Society (ECS) to attend SOFC-X conference in Nara, Japan (Spring 2007).

Refereed Publications

D.Baskar, S.B.Adler, " High temperature Faraday balance for In-situ magnetic studies in perovskite oxides ",Review of Scientific Instruments, 78 (2): Art. No. 023908 (Feb 2007)

D.Baskar, S.B.Adler, "High temperature magnetic properties of La(*1-x*)Sr(*x*)CoO(*3-delta*)", Chemistry of Materials, 20(8): 2624-2628 (Apr 2008)